

GAMMA-RAYS FROM TYPE IA SUPERNOVA SN2014J

E. CHURAZOV^{1,2}, R. SUNYAEV^{1,2}, J. ISERN³, I. BIKMAEV^{4,5}, E. BRAVO⁶, N. CHUGAI⁷, S. GREBENEV¹, P. JEAN^{8,9},
J. KNÖDLSIEDER^{8,9}, F. LEBRUN¹⁰, E. KUULKERS¹¹

¹Space Research Institute (IKI), Profsovnaya 84/32, Moscow 117997, Russia

²Max Planck Institute for Astrophysics, Karl-Schwarzschild-Strasse 1, 85741 Garching, Germany

³Institut for Space Sciences (ICE-CSIC/IEEC), 08193 Bellaterra, Spain

⁴Kazan Federal University (KFU), Kremlevskaya Str., 18, Kazan, Russia

⁵Academy of Sciences of Tatarstan, Bauman Str., 20, Kazan, Russia

⁶E.T.S.A.V., Univ. Politecnica de Catalunya, Carrer Pere Serra 1-15, 08173 Sant Cugat del Valles, Spain

⁷Institute of Astronomy of the Russian Academy of Sciences, 48 Pyatnitskaya St. 119017, Moscow, Russia

⁸Université de Toulouse; UPS-OMP; IRAP; Toulouse, France

⁹CNRS; IRAP; 9 Av. colonel Roche, BP 44346, F-31028 Toulouse cedex 4, France

¹⁰APC, Univ Paris Diderot, CNRS/IN2P3, CEA/Irfu, Obs de Paris, Sorbonne Paris Cité, France and

¹¹European Space Astronomy Centre (ESA/ESAC), Science Operations Department, P.O. Box 78, 28691 Villanueva de la Cañada, Madrid, Spain

Draft version February 14, 2022

ABSTRACT

The whole set of *INTEGRAL* observations of type Ia supernova SN2014J, covering the period 19-162 days after the explosion has been analyzed. For spectral fitting the data are split into **early** and **late** periods covering days 19-35 and 50-162, respectively, optimized for ⁵⁶Ni and ⁵⁶Co lines. As expected for the **early** period much of the gamma-ray signal is confined to energies below ~ 200 keV, while for the **late** period it is most strong above 400 keV. In particular, in the **late** period ⁵⁶Co lines at 847 and 1248 keV are detected at 4.7 and 4.3 σ respectively. The lightcurves in several representative energy bands are calculated for the entire period. The resulting spectra and lightcurves are compared with a subset of models. We confirm our previous finding that the gamma-ray data are broadly consistent with the expectations for canonical 1D models, such as delayed detonation or deflagration models for a near-Chandrasekhar mass WD. Late optical spectra (day 136 after the explosion) show rather symmetric Co and Fe lines profiles, suggesting that unless the viewing angle is special, the distribution of radioactive elements is symmetric in the ejecta.

1. INTRODUCTION

A Type Ia supernova is believed to be a thermonuclear explosion of a carbon-oxygen (CO) white dwarf (Hoyle & Fowler 1960) in a binary system, (see, e.g., Hillebrandt & Niemeyer 2000; Imshennik & Dunina-Barkovskaya 2005, for a review). Most popular scenarios of the explosion include (i) a gradual increase of the mass towards Chandrasekhar limit (e.g., Whelan & Iben 1973), (ii) a merger/collision of two WDs (e.g., Iben & Tutukov 1984; Webbink 1984; Kushnir et al. 2013), (iii) an initial explosion at the surface of the sub-Chandrasekhar WD, which triggers subsequent explosion of the bulk of the material (e.g., Nomoto & Sugimoto 1977; Hoefflich & Khokhlov 1996). In all scenarios a thermonuclear runaway converts substantial fraction of CO mass into iron-group elements and the released energy powers the explosion itself. The optical light of the supernova is in turn powered by the decay of radioactive elements, synthesized during explosion. For the first year since the explosion the decay chain of ⁵⁶Ni \rightarrow ⁵⁶Co \rightarrow ⁵⁶Fe is of prime importance. As long as the expanding ejecta are optically thick for gamma-rays the bulk of the decay energy is thermalized and is re-emitted in the UV, optical and IR band. After several tens of days the ejecta become optically thin for gamma-rays making SNIa a powerful source of gamma photons.

Here we report the results of *INTEGRAL* observations of SN2014J covering a period from ~ 16 to ~ 162 days since the explosion.

The analysis of the SN2014J data obtained by *IN-*

TEGRAL has been reported in Churazov et al. (2014b) (days ~ 50 -100 since explosion), Diehl et al. (2014) (days ~ 16 -19), Isern et al. (2015) (days ~ 16 -35), see also Diehl et al. (2015). Despite of the proximity, SN2014J in gamma-rays is an extremely faint source and the expected signal is below 1% of the background. This makes the results sensitive to the adopted procedure of the background handling by different groups and lead to tension between some results. Here we have combined all *INTEGRAL* data and uniformly process them using the same procedure as in Churazov et al. (2014b). The resulting spectra and light-curves are compared with the predictions of basic type Ia models.

Current state-of-the-art 3D simulations of type Ia explosions (e.g., Seitenzahl et al. 2013; Fink et al. 2014; Moll et al. 2014) lead to a complicated distribution of burning products in the ejecta and introduce a viewing angle dependence in the predicted gamma-ray flux. However, the overall significance of the SN2014J detection in gamma-rays by *INTEGRAL* (see §3 and §5) corresponds to ~ 10 s.t.d. This precludes a very detail model-independent analysis. We therefore took a conservative approach of comparing the data with a subset of popular 1D SNIa models (see §4), some of which were used in Milne et al. (2004) for assesment of SNIa gamma-ray codes. While these models do not describe the full complexity of SNIa ejecta, they can serve as useful indicators of the most basic characteristics of the explosion, including the total mass of radioactive nickel, total mass of the ejecta and the expansion velocity. We also verify

(§5.3) if adding an extra component, corresponding to a transparent clump of radioactive Ni, on top of the best-fitting 1D model, significantly improves the fit. In §6 we make several basic consistency checks of gamma-ray and optical data, using optical observations taken quasi-simultaneously with *INTEGRAL* observations. Section 7 provides the summary of our results.

2. SN2014J IN M82

SN2014J in M82 was discovered (Fossey et al. 2014) on Jan. 21, 2014. The reconstructed (Zheng et al. 2014; Goobar et al. 2015) date of the explosion is Jan. 14.75 UT with the uncertainty of order ± 0.3 days. At the distance of M82 (~ 3.5 Mpc), this is the nearest SN Ia in several decades. The proximity of the SN2014J triggered many follow-up observations, including those by *INTEGRAL* (Kuulkers 2014).

The SN is located ~ 1 kpc from the M82 nucleus and has a strong ($A_V \sim 2$) and complicated absorption in the UV-optical band (e.g., Goobar et al. 2014; Marion et al. 2015; Amanullah et al. 2014; Foley et al. 2014; Welty et al. 2014; Patat et al. 2015; Brown et al. 2015; Kawabata et al. 2014).

From the light curves and spectra SN2014J appears to be a “normal” SNIa with no large mixing (e.g., Marion et al. 2015; Ashall et al. 2014), consistent with the delayed-detonation models. Detection of stable Ni (Friesen et al. 2014; Telesco et al. 2015) in IR suggests high density of the burning material (see, e.g., Shigeyama et al. 1992), characteristic for near-Chandrasekhar WD.

Search in X-ray, radio and optical bands (including pre-supernova observations of M82) didn’t reveal any evidence for accretion onto the WD before the explosion, any candidate for a companion star, or compelling evidence for a large amount of circumbinary material, implicitly supporting the DD scenario (Kelly et al. 2014; Nielsen et al. 2014; Margutti et al. 2014; Pérez-Torres et al. 2014), although some SD scenarios are not excluded.

In gamma-rays the first detection of SN2014J in ^{56}Co lines was reported about 50 days since the explosion (Churazov et al. 2014a). The gamma-ray signal from SN2014J was also reported in the earlier phase ~ 16 -35 days after the explosion (Isern et al. 2014; Diehl et al. 2014).

Throughout the paper we adopt the distance to M82 (and to SN2014J) of 3.5 Mpc. The recent analysis by Foley et al. (2014) suggests the distance of 3.27 ± 0.2 Mpc. This estimate is formally consistent with the $D \sim 3.53 \pm 0.26$ Mpc from Karachentsev & Kashibadze 2006 and our adopted value. Nevertheless, one should bear in mind that all fluxes and normalizations of best-fitting models can be overestimated (underestimated) by as much as $\sim 20\%$.

The only other supernova sufficiently bright to allow for detailed study in gamma-rays from ^{56}Ni and ^{56}Co decay is the Type II SN1987A in Large Magellanic Cloud. In SN1987A the down-scattered hard X-ray continuum was first seen half a year after the explosion (Sunyaev et al. 1987; Dotani et al. 1987; Sunyaev et al. 1990), while γ -ray lines of ^{56}Co were detected several months later (Matz et al. 1988; Teegarden et al. 1989). While SN2014J is more than 60 times further away from us than SN1987A, the larger amount of radioactive ^{56}Ni and less massive/opaque ejecta in type Ia supernovae made the

detection of gamma-rays from SN2014J possible.

3. *INTEGRAL* OBSERVATIONS AND BASIC DATA ANALYSIS

INTEGRAL is an ESA scientific mission dedicated to fine spectroscopy and imaging of celestial γ -ray sources in the energy range 15 keV to 10 MeV (Winkler et al. 2003).

The *INTEGRAL* data used here were accumulated during revolutions 1380-1386, 1391-1407 and 1419-1428¹, corresponding to the period ~ 16 -162 days after the explosion.

In the analysis we follow the procedures described in Churazov et al. (2014b); Isern et al. (2013) and use the data of two instruments SPI and ISGRI/IBIS on board *INTEGRAL*.

3.1. SPI

SPI is a coded mask germanium spectrometer on board *INTEGRAL*. The instrument consists of 19 individual Ge detectors, has a field of view of $\sim 30^\circ$ (at zero response), an effective area ~ 70 cm² at 0.5 MeV and energy resolution of ~ 2 keV (Vedrenne et al. 2003; Roques et al. 2003). Effective angular resolution of SPI is $\sim 2^\circ$. During SN2014J observations 15 out of 19 detectors were operating, resulting in slightly reduced sensitivity and imaging capabilities compared to initial configuration.

Periods of very high and variable background due to solar flares and passage through radiation belts were omitted from the analysis. In particular, based on the SPI anti-coincidence system count-rates, the revolutions 1389 and 1390 were completely excluded, as well as parts of revolutions 1405, 1406, 1419, 1423 and 1426. The data analysis follows the scheme implemented for the analysis of the Galactic Center positron annihilation emission (Churazov et al. 2005, 2011). We used only “single” events (Vedrenne et al. 2003) and for each detector, a linear relation between the energy and the channel number was assumed and calibrated (separately for each orbit), using the observed energies of background lines at 198, 438, 584, 882, 1764, 1779, 2223 and 2754 keV.

The flux of the supernova $S(E)$ at energy E and the background rates in individual detectors $B_i(E, t)$ were derived from a simple model of the observed rates $D_i(E, t)$ in individual SPI detectors, where i is the detector number and t is the time of observation with a typical exposure of 2000 s:

$$D_i(E, t) \approx S(E) \times R_i(E, t) + B_i(E, t). \quad (1)$$

Here $R_i(E, t)$ is the effective area for the i -th detector, as seen from the source position in a given observation. The background rate is assumed to be linearly proportional to the Ge detectors’ saturated event rate $G_{Sat}(t)$ above 8 MeV, averaged over all detectors, i.e. $B_i(E, t) = \beta_i(E)G_{Sat}(t) + C_i(E)$, where $C_i(E)$ does not depend on time. The coefficients $S(E)$, $\beta_i(E)$ and $C_i(E)$ are free parameters of the model and are obtained by minimizing χ^2 for the entire data set. Even though the number of counts in individual exposures is low, it is still possible to use a plain χ^2 approach as long as the errors are estimated using the mean count rate and the total

¹ <http://www.cosmos.esa.int/web/integral/schedule-information>

number of counts in the entire data set is large (Churazov et al. 1996). The linear nature of the model allows for straightforward estimation of statistical errors.

Despite its proximity, SN2014J is still an extremely faint source in γ -rays. Fig.1 shows the comparison of the quiescent SPI background, scaled down by a factor of 10^3 with a sample of representative models. Two models labeled “20d uniform” and “16-35d W7” show the models for the early period of SN2014J observations. The former model is based on the best-fitting 3PAR model to the SN spectra recorded between 50-100 days after explosion (Churazov et al. 2014b), recalculated for day 20. The model assumes uniform mixing of all elements, including the radioactive ^{56}Ni , across the ejecta. This model at day 20 produces prominent ^{56}Ni lines near 158 keV and 812 keV. The latter model (w7, see §4) averaged over period 16-35 days does not include mixing and it produces much fainter lines. Finally the “50-162d W7” model corresponds to later observations. The most prominent features of this model are the ^{56}Co lines at 847 and 1238 keV. Among all these features the ^{56}Co line at 1238 keV is located in the least complicated portion of the background spectrum.

The spectral redistribution matrix accounts for the instrumental line broadening estimated from the data, accumulated during SN2014J observations. We parametrize the energy resolution as a Gaussian with the energy dependent width

$$\sigma_i \approx 0.94 (E_{line}/500)^{0.115} \text{ keV}. \quad (2)$$

Compared to our previous analysis we amended the spectral redistribution matrix of SPI by including low energy tails, associated with the interactions (Compton scattering) of incoming photons inside the detector and in the surrounding material. These photons are still registered as single events in the SPI data, but their energies are lower than the true incident energy. We used the results of Monte-Carlo simulation of SPI energy/imaging response (Sturmer et al. 2003) and folded-in our procedure of spectrum reconstruction described above. For steep spectra the account for low energy tail results in a modest $\sim 10\%$ change in the spectrum normalization, while for the very hard SN2014J spectrum it produces a low energy tail which provides large contribution to the continuum, while fluxes of narrow lines remain unaffected (Fig.2). With this response matrix the Crab Nebula spectrum, observed by *INTEGRAL* made between Feb 21 and 23, 2014, is well described by a broken power law obtained by Jourdain & Roques (2009) for earlier Crab Nebula observations with *INTEGRAL*.

In our analysis we usually ignore the part of the spectrum at energies higher than 1350 keV, since in the energy range between 1400 and 1700 keV the instrument suffers from the enhanced detector electronic noise, while at even higher energies only weaker lines from ^{56}Co decay are expected (see Table 3 in §4.2). The convolution of the fiducial SNIa model (see §4) with the simulated SPI response (Sturmer et al. 2003) confirmed that the contribution of high energy lines is negligible below 1350 keV, at least for “single” events considered here.

The inspection of Fig.1 shows that there is no chance to detect continuum in the SPI data for any of our fiducial models. E.g., for a 100 keV wide energy bin between 600

and 700 keV the expected S/N after 4 Msec observation between days 50 and 162 is $\sim 0.5\sigma$. In the real data no evidence for significant continuum above 500 keV was found in the time-averaged spectra (see §5.1 below). As Fig. 2 the off-diagonal tail of the 847 and 1238 keV lines dominates over intrinsic SN continuum (see Fig. 2), while the line shapes and fluxes are not affected.

In general, we consider the inclusion of the off-diagonal term in the response as an improvement compared to a pure diagonal response. We used this improved response throughout the paper and at the same time in §5.1 we consider several data sets, which include or exclude the SPI data below ~ 400 keV. Inclusion of the low energy ($\lesssim 400$ keV) data boosts the S/N , while the exclusion of these data (dominated by off-diagonal continuum) makes spectral fits less prone to possible uncertainties in the off-diagonal term calibration.

To verify the whole SPI pipeline, we have done an independent analysis of the same data using the tools and procedures originally developed and tuned for SN2011fe (see Isern et al. 2013). This analysis includes energy calibration, background modeling and the background and source fluxes fitting. Verification of these steps is important since the source (SN2014J) is very faint and even subtle changes in the calibration might result in significant changes in the source spectrum. The fluxes in the 835-870 keV band were derived using these two independent pipelines for every revolution during SN2014J observations. Comparing fluxes point by point, we have found very good agreement, with the scatter well within statistical errors. The signal from SN2014J is seen in both pipelines. No systematic trends of deviations with the variations of the flux level are found. We have concluded that the results are fully consistent, within the assumptions made on the background parameterization.

3.2. ISGRI/IBIS

The primary imaging instrument inboard *INTEGRAL* is IBIS (Ubertini et al. 2003) - a coded-mask aperture telescope with the CdTe-based detector ISGRI (Lebrun et al. 2003). It has higher sensitivity to continuum emission than SPI in the 20-300 keV range² and has a spatial resolution $\sim 12'$. We note here, that neither ISGRI, nor SPI can distinguish the emission of SN2014J from the emission of any other source in M82. In particular, M82 hosts two ultra-luminous and variable sources (e.g. Sazonov et al. 2014; Bachetti et al. 2014) which contribute to the flux below ~ 50 keV. ISGRI however can easily differentiate between M82 and M81, which are separated by $\sim 30'$. The energy resolution of ISGRI is $\sim 10\%$ at 100 keV. The ISGRI energy calibration uses the procedure implemented in OSA 10.039. The images in broad energy bands were reconstructed using a standard mask/detector cross-correlation procedure, tuned to produce zero signal on the sky if the count rate across the detector matches the pattern expected from pure background, which was derived from the same dataset by stacking detector images. The noise in the resulting images is fully consistent with the expected level, determined by photon counting statistics. The fluxes in broad bands were calibrated using the Crab Nebula observations with *INTEGRAL* made between Feb 21 and

² <http://www.cosmos.esa.int/web/integral/ao13>

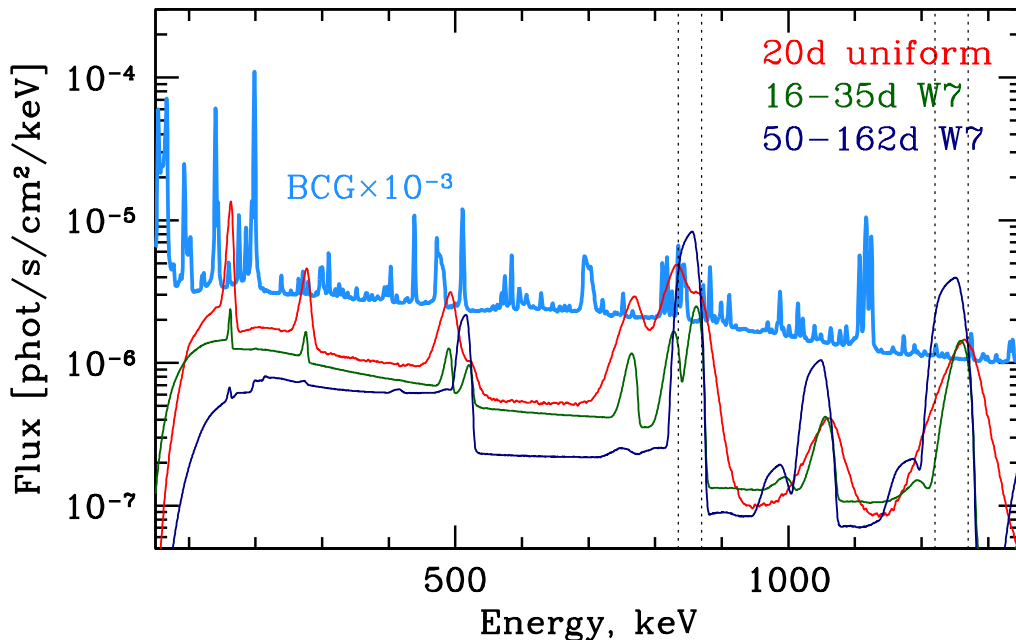


FIG. 1.— SPI quiescent background in comparison with the representative model spectra. SPI background is multiplied by a factor 10^{-3} . Green and blue lines correspond to the W7 model (Nomoto et al. 1984) averaged over the **early** and **late** periods (see §3.3), respectively. Red line shows the model the 3PAR model from Churazov et al. (2014b) for day 20 since the explosion. In this model all elements, including radioactive isotopes, are mixed uniformly over entire ejecta. The robust prediction of all plausible models is the presence of two ^{56}Co line at 847 and 1238 keV during the late phase. Vertical lines show two energy bands used for making images. The “cleanest” SPI background is near the 1238 keV line, where no strong instrumental lines are present.

23. The Jourdain & Roques (2009) model was assumed as a reference.

3.3. Lightcurves, Spectra and Images

The lightcurves in several energy bands were generated using IGSRI and SPI data. The time bins (~ 3 days each) correspond to individual revolutions of the satellite. Finer time bins are not practical given that the source is very faint. The lightcurves are shown in Figs. 3-4 together with a set of representative models (see §4). For the broad 100-200 keV band the conversion of the ISGRI flux using Crab spectrum as a reference is not very accurate because of the difference in the shape of the incident spectra. The conversion factor has been recalculated using several representative SN models, resulting in a modest $\sim 13\%$ correction factor, applied to the fluxes shown in Fig. 3.

In principle, the spectra can be extracted for any interval covered by the observations, e.g., for individual revolutions, as is done above for the lightcurves in several broad bands. For comparison of the observed and predicted spectra we decided to split the data into two intervals covering 16-35 and 50-162 days after the explosion, respectively (see Table 1). The gap between days 35 and 50 is partly due to a major solar flare. Below we refer to these two data sets as **early** and **late** periods.

Unlike the **early** period, when emergence of the ^{56}Ni lines strongly depends on the distribution of the radioactive Ni through the ejecta, for the **late** period the emission in ^{56}Co lines is a generic prediction of all plausible models. Two energy bands optimal for detection of the

SN signal in gamma-rays are clear from Fig. 1. These two bands, containing the most prominent ^{56}Co lines, were used to generate images. The images were extracted from SPI data from the **late** period as in (Churazov et al. 2014b). Namely, we vary the assumed position of the source and repeat the flux fitting procedure (see §3.1) for each position. The resulting images of the signal-to-noise ratio in the 835-870 and 1220-1270 keV energy bands are shown in Fig. 6. In both energy bands the highest peaks (4.7 and 4.3σ respectively) coincide well (within 0.3°) with the SN2014J position, marked by a cross.

The ISGRI spectra extracted at the known position of SN2014J for the **early** and **late** period are shown in Fig. 7. Low energy (less than ~ 70 keV) part of the extracted spectrum is likely contaminated by other sources in M82.

4. MODELS

4.1. A set of representative models

For comparison with the *INTEGRAL* data we used a set of representative 1D models (Table 2), based on calculations of explosive nucleosynthesis models. To the first approximation, these models are characterized by the amount of radioactive nickel, total mass of the ejecta and the expansion velocity. Although current state-of-the-art simulations of type Ia explosions can be done in 3D (e.g., Seitenzahl et al. 2013; Fink et al. 2014; Moll et al. 2014), using these models would introduce an additional viewing angle dependence. In order to avoid this extra degree of freedom and given that the overall

TABLE 1
DATA SETS

Set	Dates	Days since explosion	Exposure ^α , Msec
early	2014-01-31 : 2014-02-20	16 : 35	1.0
late	2014-03-05 : 2014-06-25	50 : 162	4.3

^α Corrected for the periods of high background and the dead-time of SPI

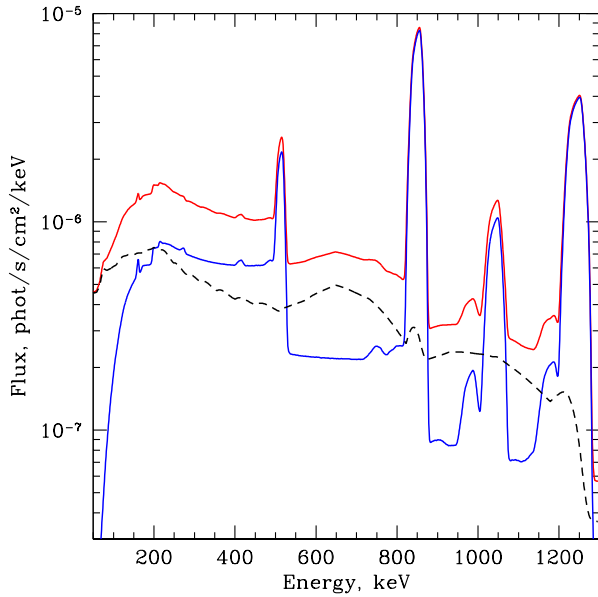


FIG. 2.— Estimated contribution of the off-diagonal terms in the SPI spectral response to the SN spectrum. The blue line shows the predicted spectrum of the W7 model for the **late** period, convolved with a simplified (nearly diagonal) SPI response. In this approximation the instrumental broadening is parametrized as an energy dependent Gaussian with the width according to eq.2. The red line shows the same spectrum convolved with the response which includes estimated off-diagonal terms, caused by Compton scattering of incident photons in the detector and surrounding structures. The off-diagonal component alone is shown with the dashed black line. The off-diagonal terms create a long low-energy tails associated with gamma-ray lines. The impact on the brightest lines is small, while the continuum is strongly affected, especially at low energies. The model W7 is averaged over the period 50-162 days after the explosion.

TABLE 2
SET OF MODELS USED IN THE PAPER

Model	M_{Ni} , M_{\odot}	M_{tot} , M_{\odot}	E_K , 10^{51} erg
DDT1p1	0.54	1.36	1.29
DDT1p4halo	0.62	1.55	1.3
DDTe	0.51	1.37	1.09
DETO	1.16	1.38	1.44
HED6	0.26	0.77	0.72
W7	0.59	1.38	1.24
ddt1p4	0.66	1.36	1.35
3Dbbal	0.66+0.04 ^α	1.36	1.35
DD4	0.61	1.39	1.24

^α additional “plume” of ⁵⁶Ni.

significance of the SN2014J detection in gamma-rays by *INTEGRAL* (see §3 and §5) corresponds to only ~ 10 s.t.d., we decided to keep in this work only a set of 1D models to confront with the data.

The set of models includes the deflagration model W7 (Nomoto et al. 1984), pure detonation model DETO (Badenes et al. 2003), the sub-Chandrasekhar model HED6 (Hoeftlich & Khokhlov 1996), and several variants of the delayed detonation models: DD4 (Woosley & Weaver 1991), DDTe (Badenes et al. 2003), DDT1p1, DDT1p4halo, ddt1p4, 3Dbbal (Isern et al. 2015). The ddt1p4 model was built to match the mass of ⁵⁶Ni suggested by the early optical evolution of SN2014J as detected with the OMC of *INTEGRAL* (Isern et al. (2014); P. Hofflich, private communication). In it, the transition density from deflagration to detonation was fixed at $1.4 \cdot 10^7$ g cm⁻³. Model DDT1p4halo is a variant of the later in which the white dwarf is surrounded by a $0.2 M_{\odot}$ envelope, as might result from a delayed merger explosion. The 3Dbbal model is essentially the same as the ddt1p4 plus a plume of $0.04 M_{\odot}$ of radioactive ⁵⁶Ni receding from the observer (see Isern et al. 2015, for details).

The emerging X-ray and gamma-ray radiation from the expanding SNIa is determined by the total amount of radioactive isotopes, their distribution over velocities, the mass and the chemical composition of the ejecta and expansion rate. The processes are essentially the same as in type II supernovae (see, e.g. Sunyaev et al. 1987, for a prototypical example of type II supernova - SN1987A). However, the mass of the ejecta and expansion rate differ strongly leading to much earlier and stronger signal in gamma-rays (see, e.g. Clayton et al. 1969; Woosley et al. 1981; Ambwani & Sutherland 1988). A comprehensive set of computations of the expected gamma-ray flux for different representative models was presented in The & Burrows (2014).

Here we use the results of similar calculations (see below), which account for line broadening, needed for systematic comparison with the *INTEGRAL* data.

A Monte-Carlo code follows the propagation of the γ -photons through the ejecta and accounts for scattering and photoabsorption of photons and annihilation of positrons. The predicted spectra were generated with a time step of one day, covering the entire observational period. These model spectra were then averaged over the periods of 16-35 and 50-162 days respectively, to provide fair comparison with the *INTEGRAL* results for the **early** and **late** periods. In particular, the effect of varying opacity in each model over the observational period is correctly captured by this procedure. The computations include full treatment of Compton scattering (coherent and incoherent), photoabsorption and pair production (see Milne et al. 2004, for details). The positrons produced by β^+ decay of ⁵⁶Co (19% of all decays) annihilate in place via positronium formation. Both two-photon annihilation into the 511 keV line and the orthopositronium continuum are included.

4.2. Transparent ejecta model (TEM)

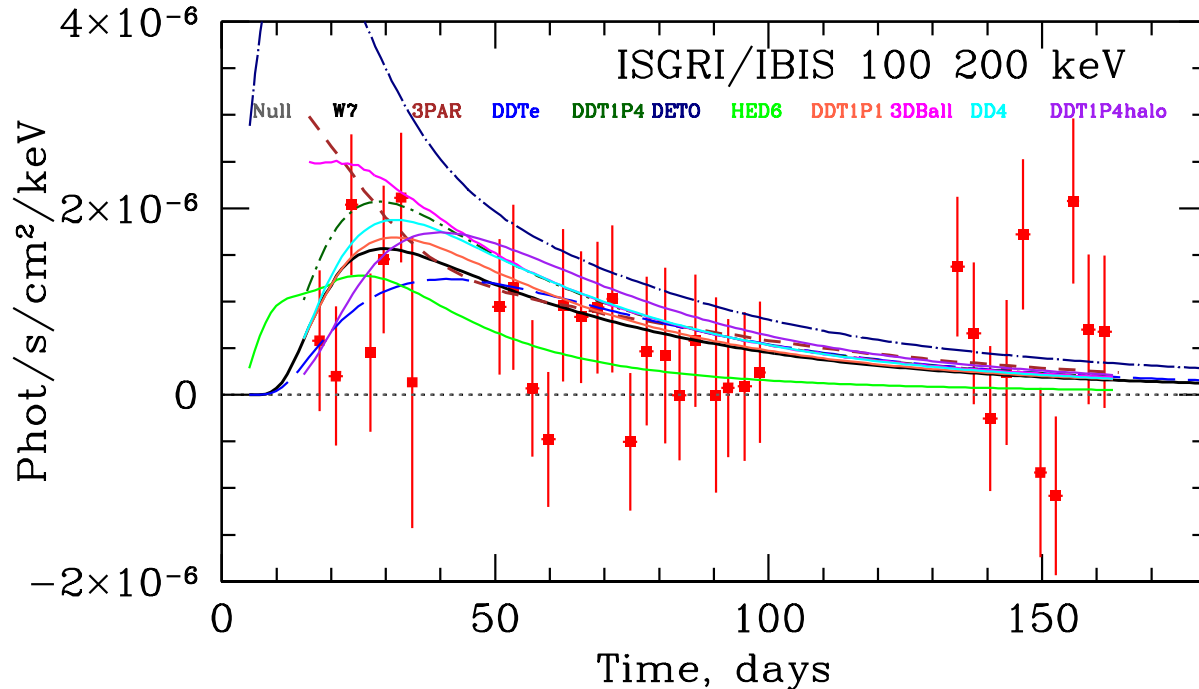


FIG. 3.— ISGRI light curve in the 100-200 keV band. The S/N ratio in this band is expected to be the highest for the plausible models. The curves show the expected flux evolution for a set of models (see §4). Color coding is explained in the legend.

As we discuss below (§5) the *INTEGRAL* data are broadly consistent with the subset of models listed in Table 2. However, Diehl et al. (2014) reported an evidence of ^{56}Ni at the surface in the first observations of SN2014J with *INTEGRAL* (see also Isern et al. 2015, for an alternative analysis of early SN2014J observations). Presence of radioactive material at the surface would be an important result, since traditional models, listed in Table 2 do not predict it. One can attempt to patch our 1D models with an additional component describing an extra radioactive material at the surface. Assuming that the material at the surface is transparent to gamma-rays, the fluxes of individual lines associated with Ni and Co decay, their energies and widths can be tied together. The transparency assumption is justified by the large velocities and small initial densities expected for matter at the surface of supernovae ejecta. In any case, it provides a lower limit to the mass of radioactive material, as opacity would demand a larger gamma-ray production rate in order to explain a given gamma-ray flux. This approach allows to describe many lines, associated with a transparent clump with only 3 parameters. Below we refer to this component as a Transparent Ejecta model (TEM), and use it in combination with the best-performing W7 model from our default set 1D models (see §4.1), i.e., the data are compared with the predictions of W7+TEM model. While this model by itself is not selfconsistent, it

can be used to answer the following questions:

- Once the predicted signal for the W7 model is removed from the observed spectra, do residuals resemble a signal expected from a transparent clump of radioactive material?
- Given the statistics accumulated by *INTEGRAL*, how much radioactive material in a transparent clump can be “hidden” in the data on top of a given 1D model?

In this section we describe the TEM model and then apply it to the data in §5.3.

The TEM model assumes that all line energies are shifted proportionally to their energies (i.e., the same velocity structure for all lines), while their flux ratios follow the predicted ratios (Nadyozhin 1994) based on the decay chains of $^{56}\text{Ni} \rightarrow ^{56}\text{Co} \rightarrow ^{56}\text{Fe}$ and $^{57}\text{Ni} \rightarrow ^{57}\text{Co} \rightarrow ^{57}\text{Fe}$. The list of the lines and their fluxes normalized to $1 M_{\odot}$ of ^{56}Ni are given in Table 3. For a given time period the model has 3 parameters: the initial ^{56}Ni mass (M_{Ni}), energy/redshift of the 847 keV line (E_{847}) and the broadening of the 847 keV line (σ_{847}). The width of each line (Gaussian σ) is defined as

$$\sigma_{\text{line}} = \sigma_{847} \times \left(\frac{E_{\text{line}}}{E_{847}} \right). \quad (3)$$

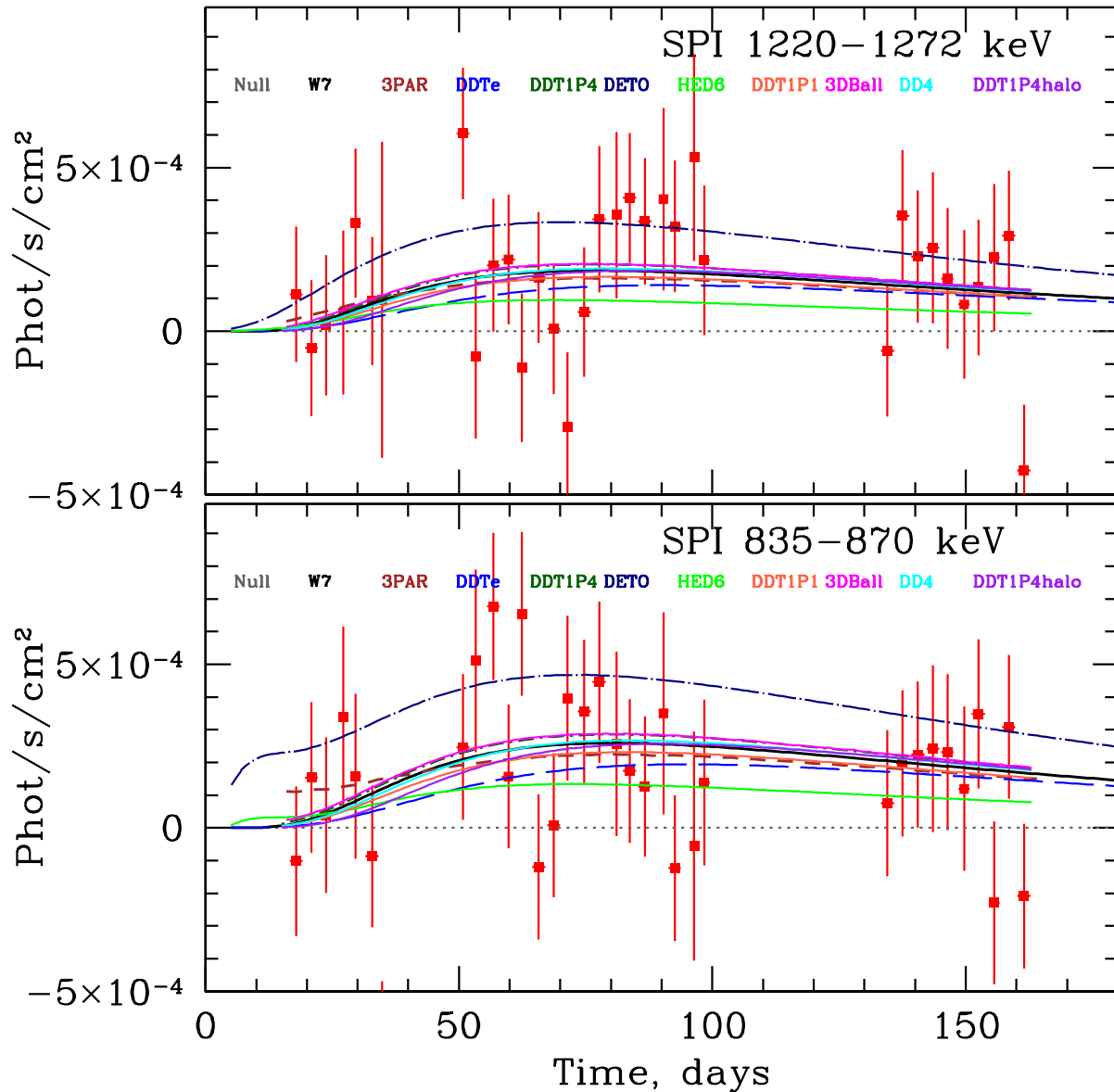


FIG. 4.— The same as in Fig.3 for SPI data in two narrow bands near the brightest ^{56}Co lines.

Ortho-positronium continuum and pair production by gamma-ray photons are neglected, while the 511 keV line is added assuming that 19% of ^{56}Co decays produce positrons, of which 25% form para-positronium yielding two 511 keV photons.

5. RESULTS

5.1. Combined ISGRI+SPI spectrum

The SPI images (Fig.6) for **late** period unambiguously show the characteristic signatures of ^{56}Co decay from SN2014J. A more quantitative statement on the amount of ^{56}Ni synthesized during explosion and on the properties of the ejecta can be obtained from the comparison of the data with the predictions of the models. Since

the **late** period is less affected by the transparency of the ejecta we start our analysis with the total spectrum obtained by *INTEGRAL* over this period.

5.1.1. Late data

The results of fitting of the combined ISGRI+SPI spectrum (Fig.8) for the **late** period are given in Table 4. A full set of models from Tab.2 is used. The two groups of columns in Table 4 differ by the energy range in the SPI data used for comparison with the model. In the first group the data of ISGRI (70–600 keV) and SPI (400–1350 keV) are used. The data below 70 keV are likely contaminated by other sources in M82. The SPI data below 400 keV are omitted since during the **late** period the

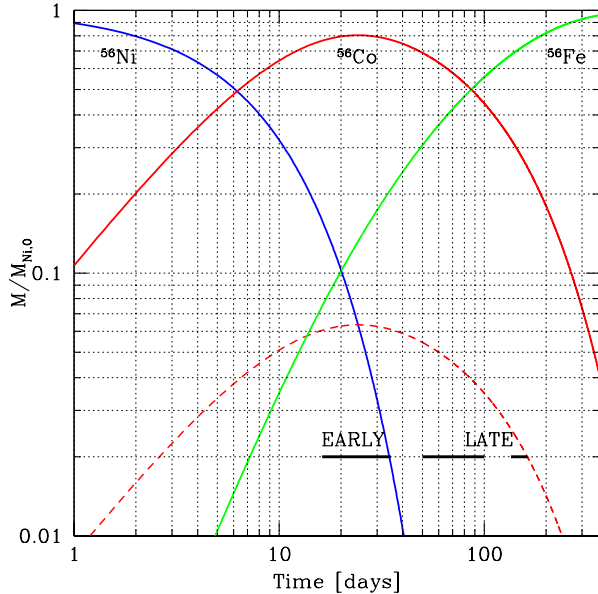


FIG. 5.— **early** and **late** periods of *INTEGRAL* observations used for spectra extraction, shown as thick horizontal bars. Three curves show the evolution of the ^{56}Ni , ^{56}Co and ^{56}Fe masses, respectively, normalized to the initial ^{56}Ni mass. Note that opacity effects tend to suppress the emergence of gamma-rays at early phases of the supernova evolution, unless radioactive isotopes are present in the outer layers of the ejecta, or the explosion is strongly asymmetric. The dashed red line shows the ^{56}Co mass scaled down by the ratio of Co and Ni decay times $\tau_{\text{Co}}/\tau_{\text{Ni}}$, which allows one to compare the expected relative strength of Ni (blue curve) and Co (dashed red curve) gamma-ray lines as a function of time.

TABLE 3
LINE FLUXES AVERAGED OVER DAYS 50-162 FOR A
TRANSPARENT EJECTA MODEL (TEM) FOR THE
INITIAL $1 M_{\odot}$ OF ^{56}Ni

E_{line} , keV	F_{line}/F_{847}	Flux ^a	Isotope
846.78	1.00	$6.57 \cdot 10^{-4}$	^{56}Co
158.38	$7.98 \cdot 10^{-3}$	$5.25 \cdot 10^{-6}$	^{56}Ni
1561.80	$1.12 \cdot 10^{-3}$	$7.34 \cdot 10^{-7}$	^{56}Ni
749.95	$3.99 \cdot 10^{-3}$	$2.62 \cdot 10^{-6}$	^{56}Ni
269.50	$2.87 \cdot 10^{-3}$	$1.89 \cdot 10^{-6}$	^{56}Ni
480.44	$2.87 \cdot 10^{-3}$	$1.89 \cdot 10^{-6}$	^{56}Ni
811.85	$6.86 \cdot 10^{-3}$	$4.51 \cdot 10^{-6}$	^{56}Ni
511.00	$9.50 \cdot 10^{-2}$	$6.24 \cdot 10^{-5}$	^{56}Co
1037.83	$1.40 \cdot 10^{-1}$	$9.20 \cdot 10^{-5}$	^{56}Co
1238.28	$6.80 \cdot 10^{-1}$	$4.47 \cdot 10^{-4}$	^{56}Co
*1771.49	$1.60 \cdot 10^{-1}$	$1.05 \cdot 10^{-4}$	^{56}Co
*2034.92	$7.90 \cdot 10^{-2}$	$5.19 \cdot 10^{-5}$	^{56}Co
*2598.58	$1.69 \cdot 10^{-1}$	$1.11 \cdot 10^{-4}$	^{56}Co
*3253.60	$7.40 \cdot 10^{-2}$	$4.86 \cdot 10^{-5}$	^{56}Co
*14.41	$1.19 \cdot 10^{-3}$	$7.80 \cdot 10^{-7}$	^{57}Co
122.06	$1.03 \cdot 10^{-2}$	$6.79 \cdot 10^{-6}$	^{57}Co
136.47	$1.19 \cdot 10^{-3}$	$7.80 \cdot 10^{-7}$	^{57}Co

NOTE. — ^a - Flux is in units of $\text{phot s}^{-1} \text{cm}^{-2}$
* - Line is outside the energy range used for fitting

data at these energies are expected to be dominated by the off-diagonal response of SPI. I.e. the observed SPI spectrum below 500 keV includes significant contribution of the gamma-ray photons at higher energies, which are down-scattered inside the body of the telescope (see Fig.2). The Null model (no source) gives $\chi^2 = 1945.38$ for 1906 spectral bins. The improvement of the χ^2 relative to the Null is calculated by fixing the normalization at the predicted value for $D = 3.5$ Mpc (column 2) and by letting it free (columns 3 and 4). The typical value of the $\Delta\chi^2 \sim 65$ suggests $\sim 8 \sigma$ detection.

One can draw two conclusions from this exercise. First of all a set of canonical 1D deflagration (w7) or delayed detonation models (e.g., DD4) fit the data well without any adjustments to the normalization. The pure detonation model DETO and a sub-Chandrasekhar model HED6 give poor fit and overproduce/underproduce the observed flux, respectively. Secondly, once the normalization is allowed to vary, all models give almost identical gain in the χ^2 , suggesting that relative strength of all prominent features is comparable in all models. Given the uncertainty in the distance to SN2014J (or M82) a deviation of the normalization at the level of $\sim 20\%$ can not be excluded. But DETO and HED6 models require by far larger changes in the normalization.

While in the above analysis the SPI data with $E < 400$ keV have been omitted to concentrate on the data less affected by the off-diagonal response, the right part of Tab.4 extends the analysis down to 70 keV for both instruments. The basic conclusions remain the same, although, as expected, the significance of the detection increases to $\gtrsim 9 \sigma$.

5.1.2. Early data

We now proceed with the same analysis of the **early** data. Table 5 contains the gain in the χ^2 for the same set of models.

The DETO is clearly inconsistent with the data - inclusion of the model increases the χ^2 relative to the Null model (no source). The HED6 model, which gave a poor fit to the **late** data, yields the χ^2 comparable to other models. This is because smaller amount of ^{56}Ni is compensated by larger transparency of the lower-mass ejecta, which is important for the **early** data.

The 3Dbba1 model gives poor gain in χ^2 if the normalization is fixed and the SPI data below 400 keV are excluded. If the normalization is free, and, especially, if the SPI data below 400 keV are included, this model performs marginally better than other models. However, it performs significantly better than other models when the SPI data below 400 keV are included. This is not surprising, since 3Dbba1 model has been designed to fit the SPI data during this period (see Isern et al. 2015, for details). The different “ranking” of the 3Dbba1 model seen in Table 5 when SPI data below 400 keV are included or excluded, suggests a tension in the comparison of the fixed-normalization 3Dbba1 model with the SPI and ISGRI data and also with the SPI data below and above 400 keV (see below).

5.1.3. Early and Late data together

Finally, in Table 6 we compare jointly the **early** and **late** data of ISGRI and SPI with the models, calculated

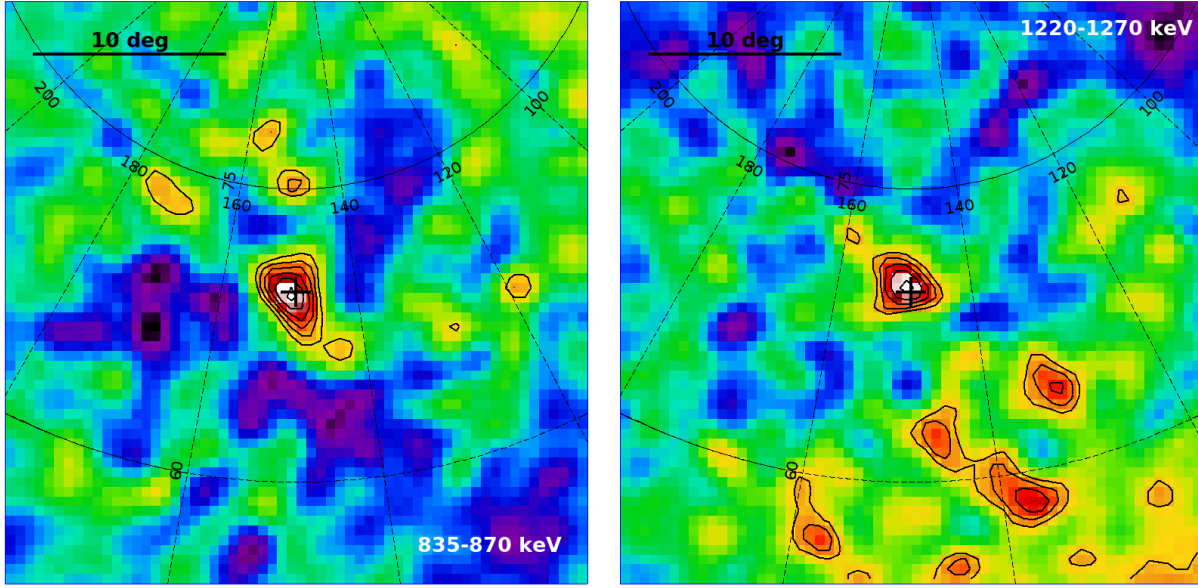


FIG. 6.— SPI images (S/N ratio) during **late** period in two narrow bands around most prominent ^{56}Co lines. Contours are at 2, 2.5 ... 5 σ . Cross shows the position of SN2014J. The brightest peaks in each image coincide well with the position of SN2014J. Due to the dither pattern^a used during observations of SN2014J the central part of the image is much better covered than the outer regions. It is therefore not surprising that the level of noise is increasing away from the nominal target.

^a<http://www.cosmos.esa.int/web/integral>

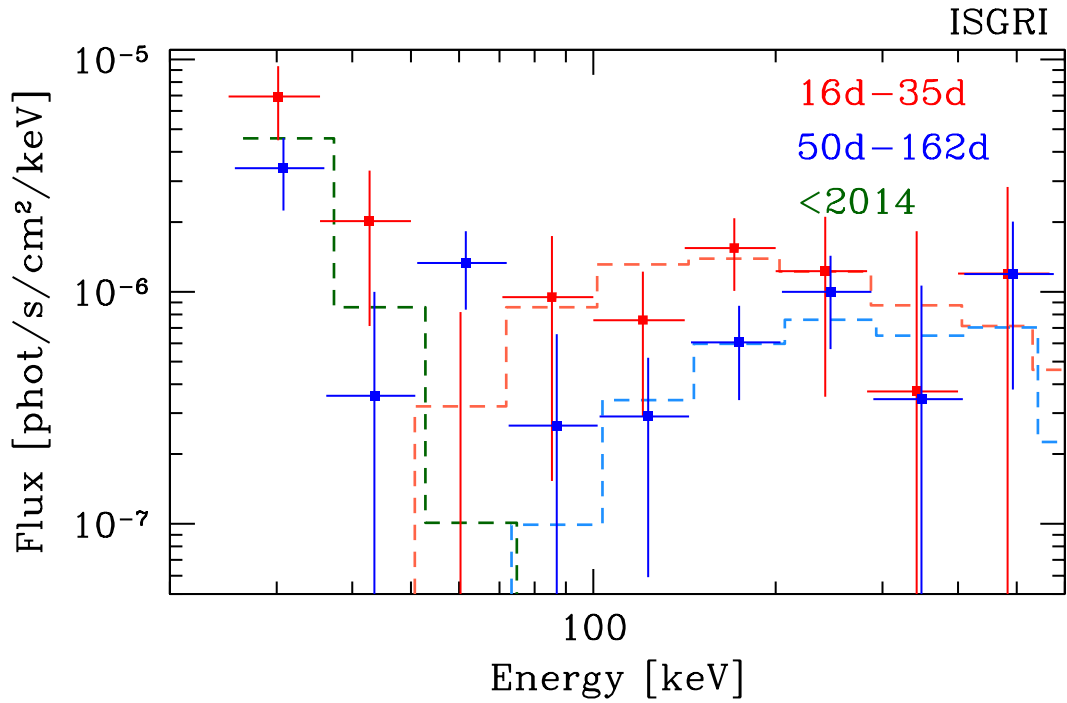


FIG. 7.— ISGRI spectrum measured at the position of SN2014J during **early** (red) and **late** (blue) periods. The energies of the second set of points are multiplied by a factor 1.02 for the sake of clarity. Dashed histograms show the predicted spectra of the W7 model for the same periods. The agreement with the predictions is reasonable except for the energies lower than ~ 70 keV, where the spectrum is likely contaminated by other sources in M82 (see, e.g. Sazonov et al. 2014). Dark green line shows crude approximation of the M82 spectrum measured before 2014.

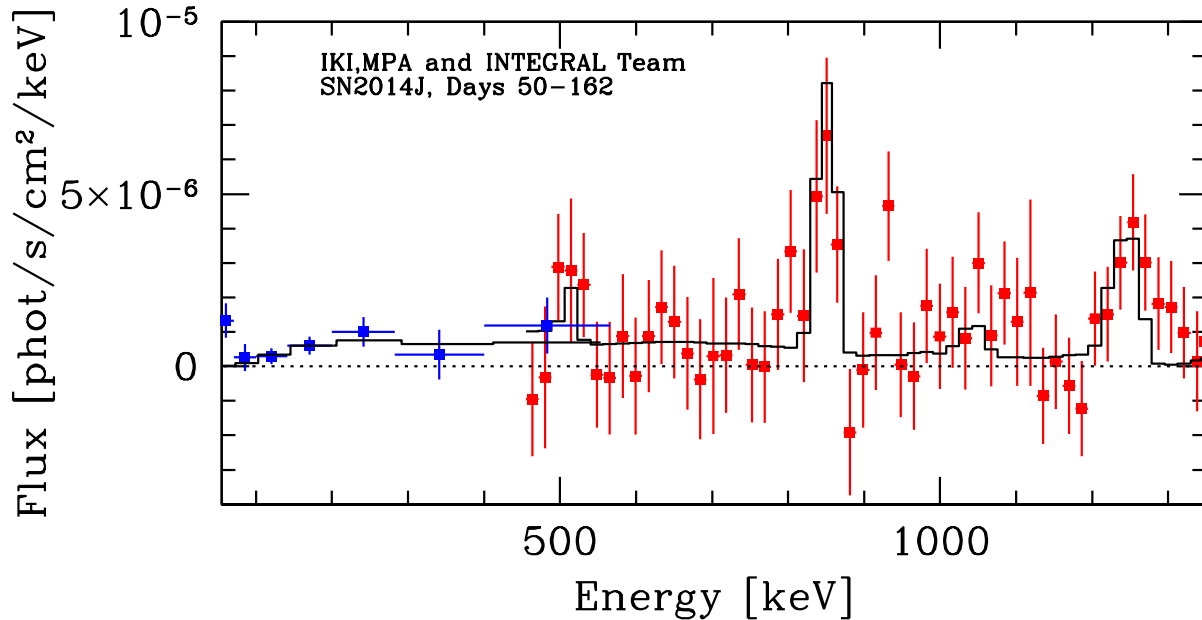


FIG. 8.— Combined ISGRI/SPI spectrum for the **late** period. The model (w7, see Tab.2) has been convolved with the SPI off-diagonal response. The SPI data below 450 keV are omitted since during **late** period the data at these energies are expected to be dominated by the off-diagonal response of SPI.

TABLE 4
 $\Delta\chi^2$ FOR BASIC MODELS FOR FIXED AND FREE NORMALIZATION RELATIVE TO THE NULL MODEL OF NO SOURCE FOR THE **late** PERIOD.

Dataset:	ISGRI(70-600 keV)&SPI(400-1350 keV)			ISGRI(70-600 keV)&SPI(70-1350 keV)		
Model	$N = 1, \Delta\chi^2$	N_{free}	$\Delta\chi^2$	$N = 1, \Delta\chi^2$	N_{free}	$\Delta\chi^2$
DDT1p1	66.4	1.03 ± 0.13	66.5	87.3	1.09 ± 0.12	87.9
DDT1p4halo	65.9	0.89 ± 0.11	66.9	88.1	0.93 ± 0.10	88.5
DDTe	62.1	1.09 ± 0.14	62.5	82.3	1.15 ± 0.13	83.7
DETO	10.1	0.52 ± 0.06	66.4	30.2	0.55 ± 0.06	87.7
HED6	47.8	1.86 ± 0.24	60.7	60.1	2.01 ± 0.22	80.5
w7	65.0	0.94 ± 0.12	65.3	86.9	1.01 ± 0.11	86.9
ddt1p4	64.9	0.85 ± 0.10	66.9	87.4	0.90 ± 0.10	88.4
3Dbbal	63.2	0.83 ± 0.10	66.1	85.7	0.88 ± 0.09	87.5
DD4	64.7	0.89 ± 0.11	65.7	87.0	0.95 ± 0.10	87.3
No source, χ^2 (d.o.f.)	1945.4 (1906)			2696.9 (2566)		

NOTE. — N is the normalization of the model with $N = 1$ corresponding to the explosion at the distance of 3.5 Mpc. $\Delta\chi^2$ characterizes an improvement of χ^2 for a given model relative to the Null model. Larger positive values indicate that the model is describing the data significantly better than other models (see Appendix). The data below 70 keV are likely contaminated by other sources in M82. SPI data below 400 keV are omitted in the first dataset (left half of the Table) since the data at these energies are expected to be dominated by the off-diagonal response of SPI (see §3.1).

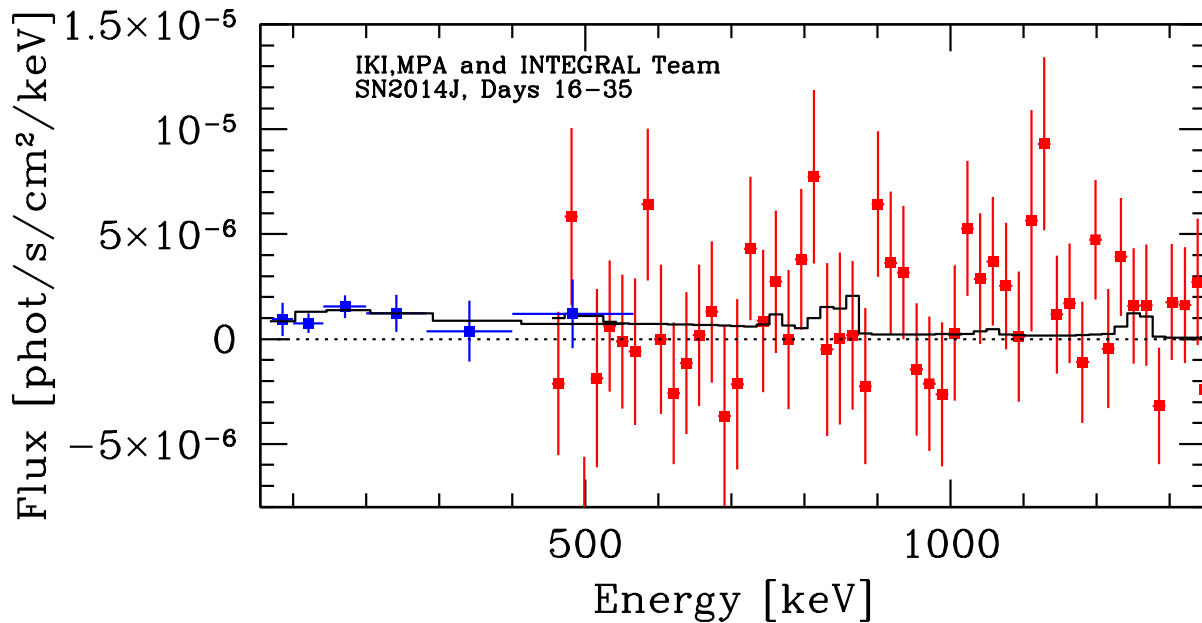


FIG. 9.— Combined ISGRI/SPI spectrum for the **early** period. The model (w7, see Tab.2) has been convolved with the SPI off-diagonal response.

TABLE 5
THE SAME AS IN TABLE 4 FOR THE **early** PERIOD.

Dataset:	ISGRI(70-600 keV)&SPI(400-1350 keV)			ISGRI(70-600 keV)&SPI(70-1350 keV)		
Model	$N = 1, \Delta\chi^2$	N_{free}	$\Delta\chi^2$	$N = 1, \Delta\chi^2$	N_{free}	$\Delta\chi^2$
DDT1p1	14.9	0.84 ± 0.21	15.4	33.2	1.11 ± 0.19	33.5
DDT1p4halo	14.6	1.00 ± 0.26	14.6	29.8	1.34 ± 0.24	31.8
DDTe	14.3	1.30 ± 0.33	15.1	26.9	1.72 ± 0.30	32.6
DETO	-83.9	0.28 ± 0.07	14.8	-64.8	0.37 ± 0.06	35.2
HED6	15.7	1.05 ± 0.26	15.8	32.7	1.39 ± 0.23	35.5
w7	15.9	0.87 ± 0.22	16.2	34.8	1.14 ± 0.19	35.3
ddt1p4	11.3	0.65 ± 0.17	15.7	33.3	0.86 ± 0.15	34.2
3Dbball	6.7	0.56 ± 0.13	17.6	37.0	0.76 ± 0.12	41.4
DD4	14.1	0.77 ± 0.19	15.5	33.6	1.01 ± 0.17	33.6
No source, χ^2 (d.o.f.)		1856.7 (1906)			2615.9 (2566)	

for corresponding periods. The two columns in Table 6 differ by the energy range in the SPI data used for comparison with the model. In each case the normalization was fixed at the value set by the adopted distance of 3.5 Mpc. In each column we mark with bold face the models which have $\Delta\chi^2$ different from the model with the largest $\Delta\chi^2$ by less than 4 (see Appendix for the clarification on the interpretation of this criterion in Bayesian and frequentist approaches). Once again, 1D deflagration model w7 and "standard" delayed detonation model perform well. The 3Dbball, which was designed to account for tentative feature in the **early** SPI data at low energies, not surprisingly performs well if the SPI data below 400 keV are included. However, if only the data

above 400 keV are used for SPI, this model yields significantly lower $\Delta\chi^2$ than the w7 or DDT1p1 models.

5.2. Comparison of gamma-ray light curves with models

While the spectra for the **early** and **late** periods already provide an overall test of the basic models, additional information can be obtained by analyzing the time variations of the fluxes in broad energy bands (see Fig.3 and 4). The total number of time bins is 34. Each bin corresponds to one revolution (i.e. ~ 3 days). The first row in Table 7 provides the values of the χ^2 (for Null model of no source) in three energy bands: 100-200 keV (ISGRI), 835-870 keV (SPI) and 1220-1272 keV (SPI). The normalization of the model lightcurves is fixed to 1.

TABLE 6
 $\Delta\chi^2$ FOR THE JOINT DATA SET OF THE **early** AND **late** SPECTRA FOR A BASIC SET OF MODELS WITH FIXED NORMALIZATION. THE VALUE OF $\Delta\chi^2$ SHOWS THE IMPROVEMENT OF THE χ^2 RELATIVE TO THE NULL MODEL OF NO SOURCE.

Model	ISGRI & SPI(400-1350 keV) $\Delta\chi^2$	ISGRI & SPI(70-1350 keV) $\Delta\chi^2$
DDT1p1	81.3	120.5
DDT1p4halo	80.5	117.8
DDTe	76.4	109.2
DETO	-73.8	-34.7
HED6	63.5	92.8
W7	80.9	121.7
ddt1p4	76.2	120.7
3Dbba11	69.9	122.7
DD4	78.8	120.7

NOTE. — Bold-faced are the models which have $\Delta\chi^2$ different from the model with the largest $\Delta\chi^2$ by less than 4, the criterion used to group models into “more plausible” and “less plausible” respectively (see Appendix).

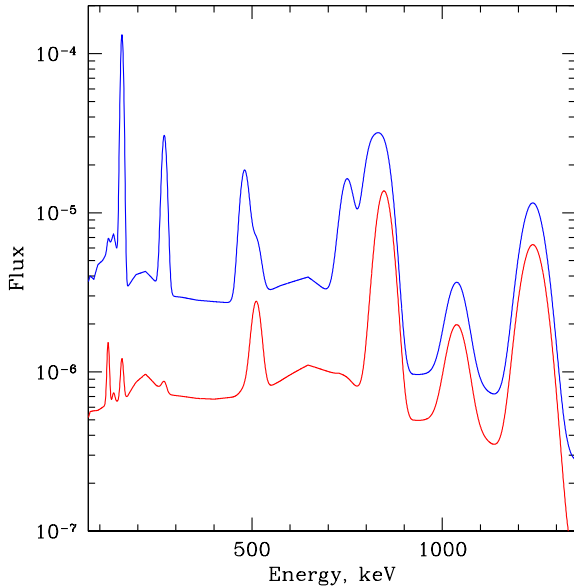


FIG. 10.— Spectra predicted by the TEM model for **early** (blue) and **late** (red) data sets, convolved with the SPI response. The broadening of the reference 847 keV line is set to 20 keV (Gaussian sigma). The initial ^{56}Ni mass is $1 M_{\odot}$.

For 34 bins the value χ^2 for a correct model is expected to be in the interval ~ 26 -42 in 68% of cases. Clearly, the Null model does not fit the data well.

Other rows show the improvement of the χ^2 relative to the Null model. I.e., $\Delta\chi^2 = \chi_{Null}^2 - \chi_{model}^2$. From Table 7 it is clear that DETO model strongly overpredicts the flux in all bands and can be excluded (χ^2 becomes worse when this model is used). Other models leads to significant improvement with respect to the Null model, except for the 3Dbba1 model in the 100-200 keV band where it exceeds the observed flux in the early observation, while in the SPI bands all these models are comparable.

The last column in Table 7 provides the χ^2 for three bands joints. This is basically the sum of the values of χ^2 for individual bands. Bold-faced are the best performing models: W7 and DDT1P1. As in §5.1 these are the models which have $\Delta\chi^2$ different from the model with the largest

$\Delta\chi^2$ by less than 4 (see Appendix).

One can also compare the lightcurves with the hypothesis of a constant flux. The mean level of flux was estimated for each band and the value of the χ^2 was calculated. The values of $\Delta\chi^2$ relative to “No source” are given in the last row of Table 7. One can see that this simple model is almost as good as other best-performing models in individual bands (even taking into account that this model has a free parameter - mean flux). This is of course the result of low statistical significance of the SN2014J detection that makes it difficult to constrain time variations of a faint signal. For the combined values for all three band the effective number of free parameter is 3 (mean fluxes in each band) and one can conclude that, e.g. W7 model performs marginally better than the constant flux model.

5.3. Search for the velocity substructure in the late data

The above analysis suggests that the *INTEGRAL* data broadly agree with a subset of simple 1D models (e.g., W7 or DD4). Since the true structure of SN2014J is surely more complicated than predicted by 1D models, it is interesting to verify if adding an extra component to the model (on top of the best-performing W7 model) significantly improves the fit. In this section we use TEM model as such extra component. This choice is partly driven by the discussion of a possible presence of ^{56}Ni at or near the surface of the ejecta in Diehl et al. (2014) and Isern et al. (2015). As described in §4.2 the TEM model described a transparent clump of radioactive Ni. All gamma-ray lines associated with the Ni \rightarrow Co \rightarrow Fe decay in the TEM model are tied to the energy (redshift) and the width of the reference 847 keV line. The flux ratios are also tied together using a model of an optically thin clump, taking into account time evolution of the Ni and Co masses. Examples of spectra predicted by TEM model (for $1 M_{\odot}$ of ^{56}Ni) are shown in Fig. 10.

Thus, we consider a composite model, consisting from the W7 model (with the normalization fixed to 1) and the TEM model. This two-component (W7+TEM) model effectively searches for a transparent clump of radioactive material on top of the base-line W7 model (see Fig.11). The horizontal axis shows the energy of the reference 847 keV line in the observer frame and different colors correspond to different 847 keV line broadening param-

TABLE 7
 $\Delta\chi^2$ FOR LIGHT-CURVES IN THREE ENERGY BANDS FOR DIFFERENT MODELS. THE VALUE OF $\Delta\chi^2$ SHOWS THE IMPROVEMENT OF THE χ^2 RELATIVE TO THE NULL MODEL OF NO SOURCE. THE VALUE OF THE χ^2 FOR THE NULL MODEL IS GIVEN IN THE FIRST RAW.

Model	100-200 keV (ISGRI)	835-870 keV (SPI)	1220-1272 keV (SPI)	Three bands jointly
No source, χ^2	51.0	49.6	51.1	151.7
DDT1P1	16.9	18.6	19.3	54.8
DDT1P4halo	9.2	17.4	19.5	46.1
DDTe	16.7	17.1	17.6	51.4
DETO	-105.0	-6.3	13.5	-97.8
HED6	20.6	16.0	14.1	50.7
W7	18.8	18.4	20.0	57.2
DDT1P4	9.1	17.5	20.3	46.9
3Dbball	-4.8	17.4	20.4	33.0
DD4	12.7	17.9	20.0	50.6
CONST	18.7	16.1	18.5	53.3

NOTE. — Total number of time bins is 34. For the joint χ^2 the effective number of bins is three times larger - 102.

eterized through a Gaussian σ - see legend. For a given redshift/energy and width of the reference 847 keV line the model has the normalization (initial ^{56}Ni mass) as the only free parameter. The best-fitting ^{56}Ni mass is shown in the top panel of Fig.11. The bottom panel (Fig.11) shows the improvement in the χ^2 (relative to the W7 model alone) due to the TEM model.

As is clear from Fig. 11 this model does not provide compelling evidence for a transparent clump on top of the W7 in the **late** data. Formally, there is a $\Delta\chi^2 \sim 9.5$ peak at ~ 858.5 keV, which corresponds to a narrow (~ 1 keV broad, red curve) component with a negative mass of $-0.05 M_\odot$, which can be interpreted as a marginal evidence for a dip in the velocity substructure, given that this improvement of the $\Delta\chi^2$ came at the cost of adding three more parameters³ to the model. One can estimate the constraints on the line flux (mass of a transparent clump) that such analysis can provide, by fixing the centroid energy and the width of the reference 847 keV line and calculating the expected statistical uncertainty. Since the normalization of the TEM model is the only free parameter in this particular experiment, the estimation of the uncertainty is straightforward (see Fig.12). Three curves shown in Fig.12 show 1σ uncertainty on the initial ^{56}Ni mass for the **early** set (dashed-blue: SPI data in the 70-1350 keV band; long-dashed-green: 400-1350 keV) and **late** set (solid-red: 400-1350 keV), respectively. Conservative upper limit based on the assumption of pure statistical errors would be 3 times these values. Letting the broadening and the redshift to be free parameters (look-elsewhere effect) would increase this limit even further.

These experiments show that the **late** data are consistent with a presence of a velocity substructure (parameterized via our TEM model) on top of the 1D W7 model at the level $\sim 0.05 M_\odot$, provided that the lines are slightly broadened.

We now do a similar experiment with the **early** data, using a TEM +W7 model for SPI data in the 400-1350 keV band (Fig.13, left panel) and in the 70-1350 keV band (Fig.13, right panel), respectively.

³ We note, that the width and especially energy of the reference line are very nonlinear parameter that could lead to large changes in the χ^2 .

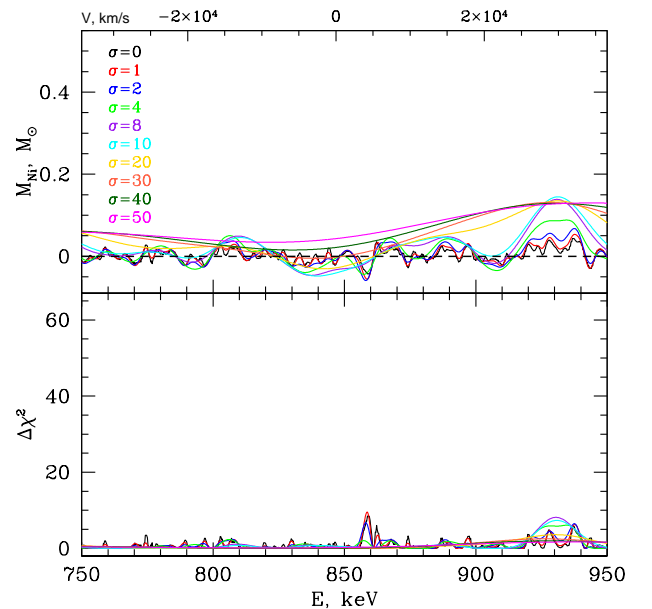


FIG. 11.— Fitting the SPI data in the 400-1350 keV band with a composite W7 + TEM model. The normalization of the W7 model is fixed to 1. In the TEM model all lines are tied to the energy (redshift) and the width of the reference 847 keV line. The flux ratios are tied using a model of optically thin clump, taking into account time evolution of the Ni and Co masses. This setup is optimized for a search of a transparent clump on top of the W7 model). For a given energy and width the model has only normalization (initial ^{56}Ni mass in the clump) as a free parameter. The bottom panel shows the improvement in χ^2 and the top panel shows the best-fitting ^{56}Ni clump mass. Different colors correspond to a different 847 keV line broadening parameterized through a Gaussian σ - see legend. No compelling evidence for a clump is seen in the data. The sensitivity of the data to the mass of the clump strongly depends on the broadening of the lines (see Fig.12).

The left panel does not show any significance evidence for a clump on top of the W7 model. The structure in the right panel is more complicated. The data used in this panel now include the ^{56}Ni line at 158 keV. We note, that if the 158 keV line is able to escape, then it is certainly true for higher energy lines of Ni and Co. Therefore the analysis should be done for the whole band to achieve

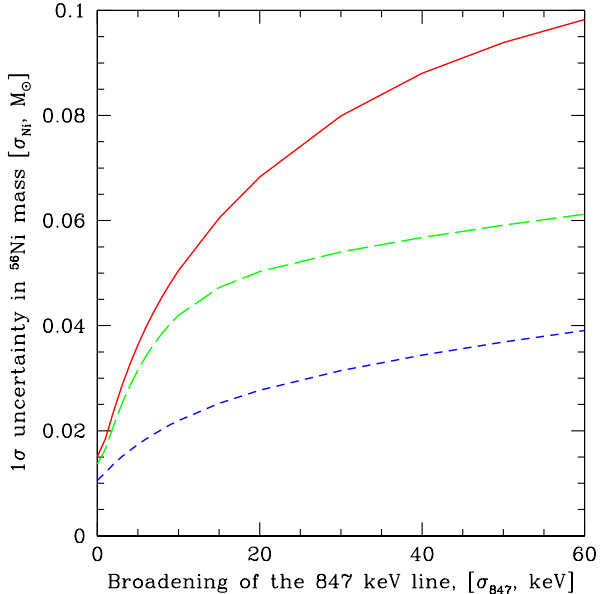


FIG. 12.— Uncertainty in the initial ^{56}Ni mass as a function of line broadening for **early** set (dashed-blue: SPI data in the 70-1350 keV band; long-dashed-green: 400-1350 keV) and **late** set (solid-red: 400-1350 keV), respectively, assuming transparency to gamma-rays generated close to the surface. A conservative upper limit on the initial mass of “extra” radioactive ^{56}Ni , is three times this value at a given line width. For the line broadening of 10^4 km s^{-1} (FWHM), the expected value of σ_{847} is $\sim 12 \text{ keV}$. This value can be regarded as a fiducial value for a simple SNIa model.

the most significant results. First of all, our analysis does not show compelling evidence for a narrow and unshifted component reported in Diehl et al. (2014) – there is a weak ($\Delta\chi^2 \sim 6$, i.e. $\sim 2.4 \sigma$ detection) if we ignore the freedom in the redshift and broadening) peak at 847.5 keV, corresponding to a narrow line (black curve) with a mass of $\sim 0.027 M_\odot$ of ^{56}Ni . There are several separate peaks of similar magnitudes, covering the energy range of interest. However there is a more significant (albeit also marginal) evidence for a redshifted and broad component with $M_{\text{Ni}} \sim 0.08 M_\odot$, $E \sim 826.5 \text{ keV}$ and $\sigma \sim 8 \text{ keV}$ (see Isern et al. 2015, for discussion). The gain in χ^2 is ~ 18 and for a fixed energy and broadening (putting under the rug possible systematic errors in the background modeling and uncertainties in the calibration of the off-diagonal response) this would be a 4.2σ detection. However the freedom in the energy, width (look elsewhere effect) and the normalization deteriorates the significance. Should all these free parameters be linear (as is normalization), one would expect the change in the χ^2 of ~ 3 due to pure statistical fluctuations. However, the energy and the width are nonlinear and the gain in χ^2 might be significantly larger. In Fig. 11 and 13 we see multiple peaks with the change/gain in χ^2 up to ~ 10 . Assuming that the latter value can be used as a crude estimate of a possible gain in χ^2 due to non-linearity of the TEM model, the significance of the detection of the excess drops below 3σ .

Taking the best-fitting parameters at the face value, we can go back to the **late** data and compare the spectra (in

the 400-1350 keV band) with the TEM +W7 model, freezing TEM model parameters at the best-fitting values obtained for the **early** data. This gives the $\chi^2 = 1883.05$, i.e. worse than the W7 model alone ($\chi^2 = 1879.3$). If we let the normalizations of both TEM and W7 models free (but freezing energy and broadening of the TEM model), then we improve slightly the χ^2 to 1878.9, but the best-fitting mass becomes slightly negative, although consistent with zero $-3 \cdot 10^{-3} \pm 5 \cdot 10^{-2} M_\odot$, while the best-fitting normalization of W7 model becomes 0.92 (c.f. Tab. 4 where SPI data are used together with the ISGRI data).

We concluded that there is a tension between “low” energy SPI data in **early** observations and the rest of the *INTEGRAL* data (Tab. 5 and Tab. 7). However, this tension is not prohibitively large and could be attributed to statistical fluctuations in the data, if a conservative approach is adopted. A possible evidence of the redshifted and broadened 158 keV line in the **early** data and possible implications are further discussed in Isern et al. (2015).

5.4. 3PAR model

Apart from the models discussed above, we also used 3PAR model, introduced in Churazov et al. (2014b). This is a spherically symmetric model of homologously expanding ejecta with exponential density profile $\rho \propto e^{v/V_e}$. The model is characterized by three parameters: initial mass of the ^{56}Ni M_{Ni} , total mass of the ejecta M_{ejecta} , and characteristic expansion velocity V_e in the exponential density distribution. In this model a mass-weighted root-mean-squared velocity of the ejecta is $\sqrt{12}V_e$.

The main shortcoming of this model is the assumption that all elements, including radioactive Ni and Co, are uniformly mixed through the entire ejecta. This is an ad-hoc assumption, made in order to stay with only three-parameters model, but it is not justified. It has the major impact for the early gamma-ray light curve, producing gamma-ray emission even at the very early phase (see Fig. 1, 3, 4). At later times (day 50 or later), the role of mixing is less significant. We therefore applied this model to the **late** ISGRI and SPI spectra to get estimates of M_{Ni} , M_{ejecta} and V_e , which are not limited to values characteristic to the set of plausible models given in Table 2. The main purpose of using this model is to understand the level of constraints provided by the *INTEGRAL* data on the main characteristics of the supernova. Simplicity of the model allows us to calculate this model on a large grid of possible values of M_{Ni} , M_{ejecta} and V_e .

A Monte Carlo radiative transfer code is used to calculate the emergent spectrum, which includes full treatment of Compton scattering (coherent and incoherent) and photoabsorption. Pair production by γ -ray photons is neglected. The positrons produced by β^+ decay annihilate in place via positronium formation. Both two-photon annihilation into the 511 keV line and the ortho-positronium continuum are included.

The results are shown in Fig. 14. The best-fitting values $M_{\text{Ni}} = 0.63 M_\odot$, $M_{\text{ejecta}} = 1.8 M_\odot$, $V_e = 3 \cdot 10^3 \text{ km s}^{-1}$ are marked with a cross. The 1σ confidence contours (corresponding to $\Delta\chi^2 = 1$, i.e. for single parameter of interest) are shown with the thick solid line. Clearly, the Ni mass M_{Ni} and the character-

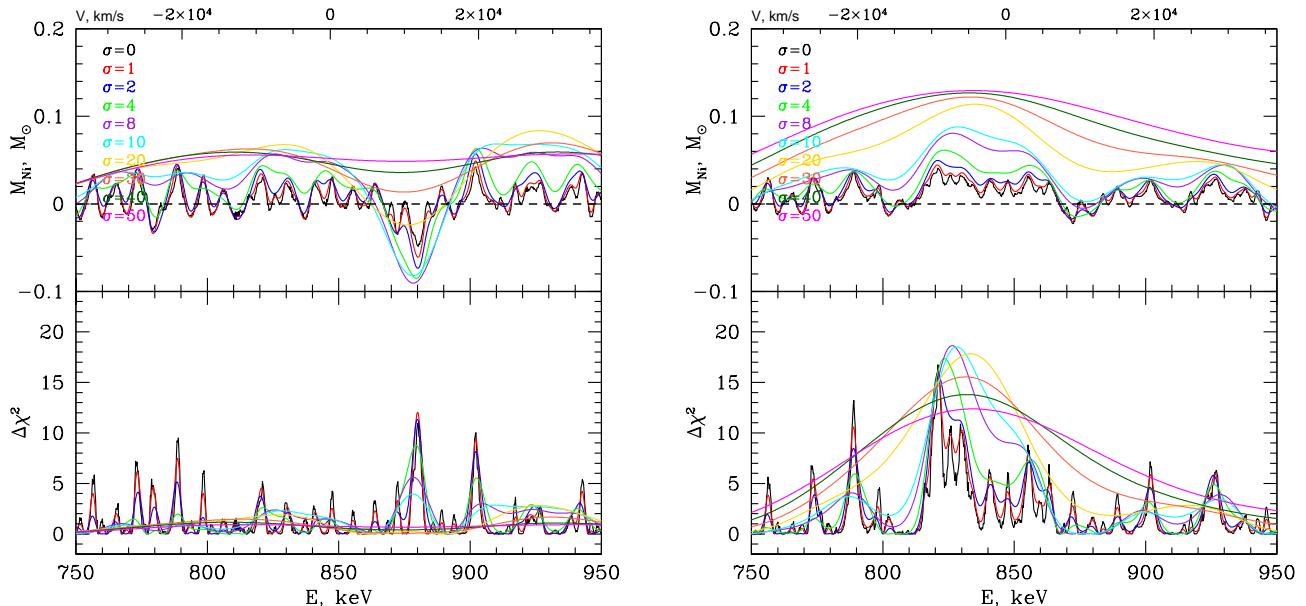


FIG. 13.— Same as in Fig.11 but for the **early** SPI spectrum. **LEFT:** TEM +W7 model and the SPI data in the 400-1350 keV band. The normalization of the W7 model is fixed to 1. **RIGHT:** TEM +W7 model and the SPI data in the 70-1350 keV band. The normalization of the W7 model is fixed to 1. The low energy part of the SPI spectrum is included to make sure that the ^{56}Ni line at 158 keV is within the energy range probed. There is a marginal evidence of a redshifted (by ~ 8000 km/s) component with the width of ~ 8 keV (Gaussian sigma), corresponding to $M_{\text{Ni}} \sim 0.08 M_{\odot}$. See text for the discussion.

istic expansion velocity V_e are better constrained than the ejecta mass. This is not surprising, given that the data averaged over the period 50-162 days after explosion are used, when the ejecta are relatively transparent for gamma-rays. As a result the flux in the lines depends primarily on the Ni mass, line broadening is set by the expansion velocity, while ejecta mass influence mostly the amplitude of the scattered component, which declines with time relative to the ortho-positronium continuum when the optical depth declines. If we fix the poorly constrained ejecta mass to $M_{\text{ejecta}} = 1.4 M_{\odot}$, then the derived Ni mass is constrained to the range 0.54-0.67 M_{\odot} .

For the set of models listed in the Table 2 we can estimate the effective V_e using the relation $V_e = \sqrt{\frac{E_K}{6M_{\text{ejecta}}}}$, valid for pure exponential model. The values V_e vary between ~ 2580 km s $^{-1}$ for DDTe to ~ 2960 km s $^{-1}$ for DETO models and is equal to 2740 km s $^{-1}$ and 2820 km s $^{-1}$ for W7 and DDT1p1 respectively. Not surprisingly all “successful” models (e.g. W7 and DDT1p1) have their characteristic parameters well inside contours plotted in Fig. 14, while DETO and HED6 are far outside the contours, primarily because of Ni mass.

5.5. Summary of model fitting

The comparison of the *INTEGRAL* data with the subset of models (see the sections above) allows one to crudely rank the models according to their success in different tests. For each test (data set) we can choose the “best” model, which provides the largest improvement $\Delta\chi^2$ compared to Null model (or having the smallest χ^2 for the lightcurves). We can then adopt an ad hoc definition that other models that have χ^2 different from the best model by 4 (i.e. $\sim 2 \sigma$ confidence) are

classified as “good”. Similar approach can be applied to the lightcurves in each band (Tab. 7), by adding 4 to the minimal value of the χ^2 among models. Applying this test to Tables 4 - 7 we conclude that W7 and DDT1p1 pass all these tests, closely followed by DD4, ddt1p4, and then by DDT1p4halo and 3Dbba1. DETO and HED6 fail most of the tests. Of course, given the uncertainties in the distance, background modeling and calibration issues, we can not reject models other than DETO and HED6. E.g., if we let the normalization to be a free parameter (equivalent of a statement that the distance is highly uncertain) then most of the models become barely distinguishable. We rather state, that a whole class of near-Chandrasekhar models provides a reasonable description of the data, with the W7 and DDT1p1 being the most successful, closely followed by a broader group of delayed-detonation models.

6. CONSISTENCY WITH OPTICAL DATA

We now make several basic consistency checks of gamma-ray and optical data, using optical observations taken quasi-simultaneously with *INTEGRAL* observations.

6.1. Optical and gamma-ray luminosities

We use *BVRIJHK* photometry reported by Foley et al. (2014) to estimate the bolometric (UVOIR) luminosity of SN 2014J on days 73 and 96 after the explosion. Since the data do not contain the *U*-band photometry, we include the *U* magnitude recovered on the bases of the *U - B* color of the dereddened normal SN Ia, SN 2003hv (Leloudas et al. 2009). The SN 2014J fluxes were corrected for the extinction using slightly different extinction laws reported by Amanullah et al. (2014) and Foley et al. (2014). The average of both fluxes for each

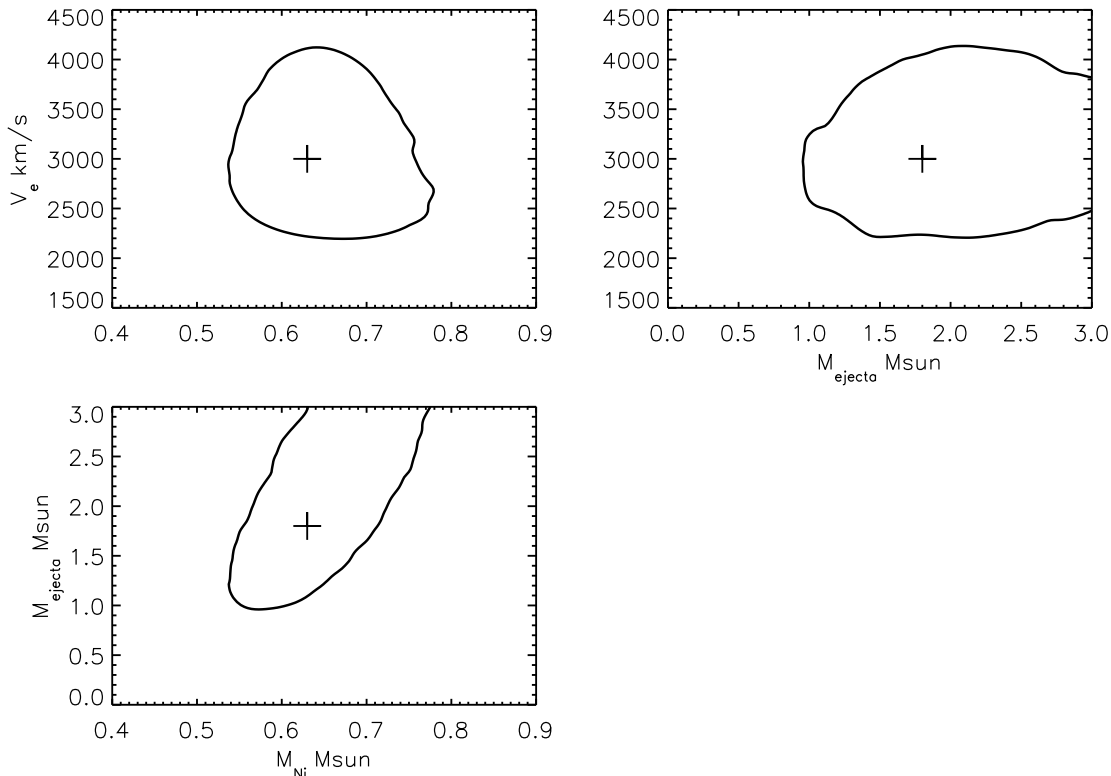


FIG. 14.— Confidence contours for 3PAR model, corresponding to $\Delta\chi^2 = 1$ with respect to the best-fitting value. The cross show the best-fitting parameters of the 3PAR model: $M_{\text{Ni}} \sim 0.63 M_{\odot}$, $v_e \sim 3000 \text{ km s}^{-1}$, $M_{\text{ejecta}} \sim 1.8 M_{\odot}$. The late ISGRI and SPI spectra are used for this analysis. Confidence intervals plotted in this figure correspond to 1σ for a single parameter of interest. The largest uncertainty is in the mass of the ejecta, while the Ni mass is the best determined quantity.

epoch were used then to produce the integrated flux. To this end we approximated the spectral energy distribution by the combination of two functions each of which is a smooth broken power law. The SED integration in the range of $0.1 < \lambda < 10 \mu\text{m}$ with the distance of 3.5 Mpc, results in the luminosity estimates of $(11 \pm 1) \times 10^{41} \text{ erg s}^{-1}$ on day 73, and $(6.5 \pm 0.6) \times 10^{41} \text{ erg s}^{-1}$ on day 96. These values agree well with the estimated amount of deposited energy in the best-fitting 3PAR model: $\sim 1.0 \times 10^{42} \text{ erg s}^{-1}$ and $\sim 5.3 \times 10^{41} \text{ erg s}^{-1}$ for day 73 and 96 respectively. According to this model the fraction of thermalized energy is $\sim 34\%$ and $\sim 20\%$ for these dates respectively.

6.2. Asymmetry in late optical spectra?

The issue of asymmetry of SN 2014J ejecta is of vital importance because the strong deviation of the ^{56}Ni distribution from the spherical symmetry would affect the interpretation of the gamma-ray data. Generally, the asymmetry of the ^{56}Ni distribution is expected in the binary WD merger scenario (Pakmor et al. 2012). Moreover, a single degenerate scenario also does not rule out the ejecta asymmetry caused by the noncentral early deflagration (Malone et al. 2014). In fact, signatures of asymmetry have been already detected in several SNe Ia

at the nebular stage ($t > 100 \text{ d}$). The asymmetry is manifested in the emission line shift or/and the double peak emission line profiles (Motohara et al. 2006; Maeda et al. 2010; Dong et al. 2014).

To probe a possible asymmetry of SN 2014J ejecta we rely on the nebular optical spectrum taken on day 119 after the B maximum, i.e., 136 d after the explosion (Bikmaev et al. 2015) at the 1.5-m Russian-Turkish telescope (RTT-150) of the TUBITAK National Observatory (Antalya, Turkey). The SN 2014J spectrum corrected for the interstellar reddening in M82 of $E(B - V) = 1$ (c.f. Foley et al. 2014) is shown in Fig. 15 together with that of SN 2011fe obtained at the same instrument on day 141 after the maximum. The spectra of both supernovae look similar except for the blueshift of SN 2011fe emissions by $\sim 10^3 \text{ km s}^{-1}$ relative to SN 2014J.

We focus on the [CoIII] 5890 Å emission that is not hampered markedly by the blending with other lines. It should be emphasised that on day 136 d after the explosion this line is dominated by ^{56}Co ; the contribution of ^{57}Co and stable Co isotopes is negligible. The Thomson optical depth at this epoch is small (~ 0.2) and does not affect the line profile. The [CoIII] emission is the superposition of five lines of the $a^4\text{F} - a^2\text{G}$ multiplet. Each line we describe by the Gaussian with the ampli-

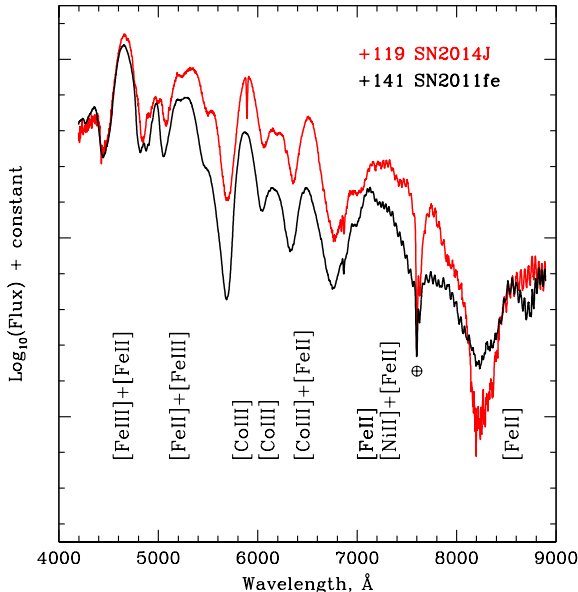


FIG. 15.— The spectra of SN 2014J (day 119 after the maximum) and SN2011fe (day 141 after the maximum) obtained with RTT-150 telescope Bikmaev et al. (2015). Overall the spectra are very similar in terms of the flux level, line shape and line ratios. The exception is the prominent blueshift of [Fe III], [Fe II], and [Co III] emissions of SN 2011fe relative to SN 2014J. The strong interstellar Na I absorption in the SN 2014J spectrum arises in the M 82 galaxy.

tude proportional to the collisional excitation rate times the radiative branching ratio. We adopt the heliocentric recession velocity of $+104 \pm 15 \text{ km s}^{-1}$ that takes into account the recession velocity of $+203 \text{ km s}^{-1}$ for M 82 (NASA Extragalactic Database NED) and the rotational velocity of M 82 at the SN 2014J position. The best fit (Fig. 16) is found for the full width at half maximum for each line $\text{FWHM} = 10450 \text{ km s}^{-1}$ and the line shift of $v_s = +130 \pm 17 \text{ km s}^{-1}$. With the exception of this small shift, each [Co III] line is fairly symmetric at least in the radial velocity range of $|v_r| < 6100 \text{ km s}^{-1}$. The small line shift may be related to either intrinsically small asymmetry of ^{56}Ni distribution, or the special viewing angle, if the ejecta is actually non-spherical. To summarize, the SN 2014J optical spectrum does not show signatures of strong asymmetry.

7. DISCUSSION AND CONCLUSIONS

We have analyzed a complete set of *INTEGRAL* observations of SN2014J. We confirm our previous results (Churazov et al. 2014b) that the data are broadly consistent with the predictions of a nearly-Chandrasekhar WD explosion, with (1D) deflagration or delayed detonation models providing equally good description (see Tables 6 - 7). While pure deflagration models are disfavored because of the expected large scale mixing and incomplete

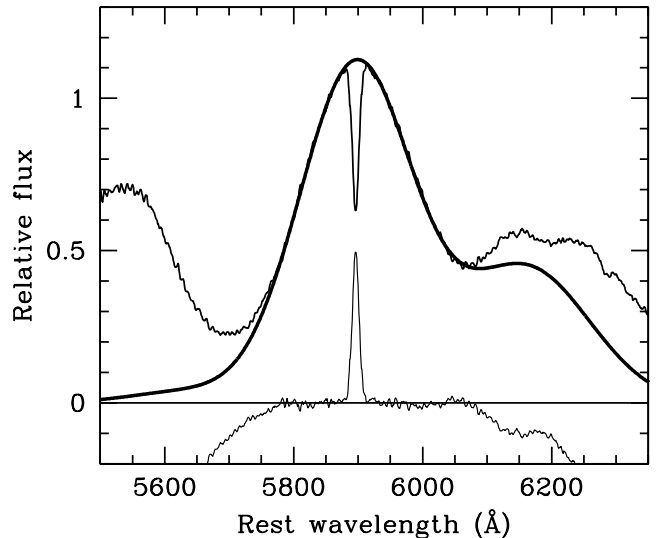


FIG. 16.— [Co III] 5900 \AA emission in the SN2014J spectrum on day 119 (**thin** line) along with the model (**thick** line) which includes five component of the $a^4\text{F} - a^2\text{G}$ multiplet. The narrow absorption feature at the top of the profile is due to Na I interstellar absorption in M 82. At the bottom shown is the residual "model minus observation", which demonstrates a good fit in the range of 5770-6060 \AA .

burning in 3D simulations, in the 1D case they yield the same gamma-ray flux as the delayed detonation models. Pure detonation (or strongly sub-Chandrasekhar) models strongly overproduce (underproduce) observed gamma-ray flux and can be excluded. Allowing a freedom in the normalization of the model (equivalent to allowing the initial mass of ^{56}Ni to be a free parameter, while keeping other parameters unchanged) makes all models essentially indistinguishable at the level of statistics, accumulated by *INTEGRAL*.

We have searched for possible velocity substructure on top of the predictions from 1D models, by adding a set of broadened Gaussian lines to the best-performing W7 model. The energies and fluxes of the lines are tied to the predictions of the Ni and Co decay chains, appropriate for the optically thin clump of Ni. This analysis did not reveal strong evidence for a prominent velocity substructure in the gamma-ray data during the late phase of the SN evolution (after day 50). Given the statistics accumulated by *INTEGRAL*, a clump with the ^{56}Ni mass $\sim 0.05 M_{\odot}$ producing slightly broadened lines (Fig.12) could be consistent with the **late** gamma-ray data. Similar analysis of the **early** data has a best-fitting solution with a redshifted and broadened component with $M_{\text{Ni}} \sim 0.08 M_{\odot}$, $E \sim 826.5 \text{ keV}$ and $\sigma \sim 8 \text{ keV}$. However, the statistical significance of this extra component is marginal and the **late** observations do not provide further evidence for the presence of such component (see

also Diehl et al. 2014; Isern et al. 2015, for independent analysis of early observations of SN2014J).

From the optical light curves and spectra SN2014J appears to be a “normal” SNIa with layered structure and no evidence for large-scale mixing (e.g., Marion et al. 2015; Ashall et al. 2014), consistent with the delayed-detonation models. The detection of stable Ni (Friesen et al. 2014; Telesco et al. 2015) in IR suggests high density of the burning material, characteristic for near-Chandrasekhar WD.

Optical spectrum taken at the nebular stage (day ~ 136 after the explosion) also do not show strong asymmetry in the Co and Fe lines. Unless the viewing angle is special, the distribution of these elements in the ejecta is symmetric. These data do not provide any direct support for collision/merger scenario. The late SN2014J spectrum is very similar to that of SN2011fe, albeit with the pronounced blueshift of emission lines of the latter.

Apart from the above mentioned feature in the **early** observation, which we consider as marginal, the rest of the *INTEGRAL* and optical data appear consistent with the predictions of “canonical” 1D explosion models of a nearly-Chandrasekhar carbon-oxygen white dwarf.

GRAL, an ESA project with instruments and a science data centre funded by ESA member states (especially the principal investigator countries: Denmark, France, Germany, Italy, Switzerland and Spain) and with the participation of Russia and the United States. We are grateful to ISOC for their scheduling efforts, and the *INTEGRAL* Users Group for their support in the observations. E.C., R.S., S.G. are partly supported by grant No. 14-22-00271 from the Russian Scientific Foundation. J.I. is supported by MINECO-FEDER and Generalitat de Catalunya grants. I.B. is partly supported by Russian Government Program of Competitive Growth of KFU. E.B. is supported by Spanish MINECO grant AYA2013-40545. The SPI project has been completed under the responsibility and leadership of CNES, France. ISGRI has been realized by CEA with the support of CNES. We thank Adam Burrows, Peter Höflich, Rishi Khatri, Ken Nomoto, Victor Utrobin, Alexey Vikhlinin and Stan Woosley for helpful discussions.

This work was based on observations with INTE-

APPENDIX

COMPARISON OF SIMPLE MODELS VIA $\Delta\chi^2$ CRITERION

In this appendix we clarify our approach of comparing different models using ungrouped spectral and/or timing data.

Grouping the data and small number of counts per bin

Consider N data points D_i , $i = 1, N$ and $N \gg 1$ (e.g., a spectrum measured in N energy bins) that correspond to a model M_i , $D_i = M_{i,i} + n_i$, where n_i is the noise with Gaussian distribution with zero mean and known variance σ_i^2 . The noise is uncorrelated, i.e. $\langle n_i n_j \rangle = 0$, if $i \neq j$. For simplicity we drop below the index i in the expressions containing summation over i .

Suppose that we want to compare two competing models M_1 and M_2 with no free parameters (this corresponds to Neyman-Pearson lemma of two simple hypotheses). For our purpose it is useful to write explicitly the probability distribution of $\Delta\chi^2$ between competing models.

Let us define $\delta_1 = M_1 - M_i$ and $\delta_2 = M_2 - M_i$ and calculate χ^2 for both models. For the model M_1

$$\chi_1^2 = \sum \left(\frac{M_1 - D}{\sigma} \right)^2 = \sum \left(\frac{\delta_1 + n}{\sigma} \right)^2 = \sum \left(\frac{\delta_1}{\sigma} \right)^2 + 2 \sum \frac{\delta_1 n}{\sigma^2} + \sum \left(\frac{n}{\sigma} \right)^2, \quad (\text{A1})$$

and a similar expression for M_2 . Thus $\Delta\chi^2 = \chi_1^2 - \chi_2^2$ is

$$\Delta\chi^2 = \sum \left(\frac{\delta_1}{\sigma} \right)^2 - \sum \left(\frac{\delta_2}{\sigma} \right)^2 + 2 \sum \frac{\delta_1 n}{\sigma^2} - 2 \sum \frac{\delta_2 n}{\sigma^2} = \quad (\text{A2})$$

$$\sum \left(\frac{\delta_1}{\sigma} \right)^2 - \sum \left(\frac{\delta_2}{\sigma} \right)^2 + 2 \sum \frac{\delta_{1,2} n}{\sigma^2}, \quad (\text{A3})$$

where $\delta_{1,2} = M_1 - M_2$. The last term in the above expression obviously has a Gaussian distribution with zero mean and variance $4 \sum \frac{\delta_{1,2}^2 \langle n^2 \rangle}{\sigma^4} = 4 \sum \frac{\delta_{1,2}^2}{\sigma^2}$. Thus

$$\Delta\chi^2 = \sum \left(\frac{\delta_1}{\sigma} \right)^2 - \sum \left(\frac{\delta_2}{\sigma} \right)^2 + X \sqrt{4 \sum \frac{\delta_{1,2}^2}{\sigma^2}}, \quad (\text{A4})$$

where X has a Normal distribution. It is clear that the above expression *does not depend on data grouping* (see

Churazov et al., 1996) as long as the grouping does not severely affect the shapes of δ_1 , δ_2 or $\delta_{1,2}$. Furthermore, $\Delta\chi^2$ can have a Gaussian distribution by the central limit theorem, even when the noise in the original data is not Gaussian. For instance, if n corresponds to the Poisson noise in the data with small number of counts per bin, the $\Delta\chi^2$ will have Gaussian distribution provided that the *total number of counts* contributing to $\sum \frac{\delta_{1,2}^n}{\sigma^2}$ is large (Churazov et al., 1996). We therefore can use the original data with no grouping to calculate $\Delta\chi^2$.

Dividing the models into a “more plausible” and “less plausible” groups

For a given observed $\Delta\chi_{obs}^2$ the ratio of likelihoods for two models is $\Lambda = \frac{L(M_1)}{L(M_2)} = e^{-\Delta\chi_{obs}^2/2}$, which corresponds to the Akaike information criterion (AIC) or Bayesian information criterion (BIC) criteria. Alternatively we can also employ Neyman-Pearson lemma to differentiate between two models. If M_1 is the true model, then $M_1 = M_t$, $\delta_1 = 0$, $\delta_2 = -\delta_{1,2}$ and the distribution of $\Delta\chi^2 = \chi_1^2 - \chi_2^2$ is

$$\Delta\chi^2 = -\sum \left(\frac{\delta_{1,2}}{\sigma}\right)^2 + X\sqrt{4\sum \frac{\delta_{1,2}^2}{\sigma^2}}. \quad (\text{A5})$$

Then the probability α of getting $\Delta\chi^2 > y$ is

$$\alpha = Q(x), \quad (\text{A6})$$

where $Q(x) = 1/2 \operatorname{erfc}(x/\sqrt{2})$, $x = \frac{A+y}{2\sqrt{A}}$ and $A = \sum \left(\frac{\delta_{1,2}}{\sigma}\right)^2$. Although the value of A is known, we can take a conservative approach and write that $\frac{A+y}{2\sqrt{A}} \geq \sqrt{y}$ for any $A \in [0, \infty]$. This value is achieved at $A = y$. Thus one can conclude that the conservative estimate of the probability of getting better χ^2 for the wrong model (i.e., $\Delta\chi_{obs}^2 > y$) corresponds to more than \sqrt{y} standard deviations. In the paper we use the value of $\Delta\chi_{obs}^2 < 4$ to separate the models into a “more plausible” and “less plausible” groups. As we emphasized above, one can also interpret this value in the frame of BIC or AIC approaches.

Pairwise model comparison and the goodness of fit criterion

When comparing two models in terms of the χ^2 we are effectively projecting the N -dimensional data D on a line connecting the models M_1 and M_2 . We can formally introduce a linear parameter p , make a composite model $M_1 + p(M_2 - M_1)$ and calculate best-fitting value p_{bf} that minimizes the χ^2

$$p_{bf} = \frac{\sum -(D - M_1)\delta_{1,2}/\sigma^2}{\sum \delta_{1,2}^2/\sigma^2}. \quad (\text{A7})$$

It is obvious that this quantity has a Gaussian distribution with the standard deviation

$$\sigma_p = \left(\sum \delta_{1,2}^2/\sigma^2\right)^{-1/2}. \quad (\text{A8})$$

We can now use the deviation of p_{bf} from 0 or 1 as a goodness of fit criterion for models M_1 and M_2 , respectively. A significant deviation (i.e. $|p_{bf}/\sigma_p| \gg 1$ or $|(p_{bf} - 1)/\sigma_p| \gg 1$) implies that one of the models (or both) is unlikely. While the goodness of fit can be calculated for each model alone, the power of the criterion depends on the data grouping (imagine, for example, a very weak signal distributed over a large number of bins). The goodness of fit calculation described above verifies only the projection of the data on the line set by models, but it “optimally” compares the difference between plausible models with the signal present in the data.

For each model used in §4 we have calculated the maximum deviation $|p_{bf}/\sigma_p|$ with respect to all other models (except for the **3Dbba1** model that was designed to fit the *INTEGRAL* data). Table 8 provides corresponding values, when ISGRI and SPI data for the **early** and **late** periods are considered jointly. Based on this analysis we conclude that **No source**, **DETO**, **HED6** and (marginally) **DDTe** models are disfavored by the data, while other models are compatible with the data.

REFERENCES

- | | |
|---|--|
| <p>Achtermann, J. M. & Lacy, J. H. 1995, ApJ, 439, 163
 Arnett, W. D. 1982, ApJ, 253, 785
 Amanullah, R., Goobar, A., Johansson, J., et al. 2014, ApJ, 788, L21
 Ambwani, K., & Sutherland, P. 1988, ApJ, 325, 820
 Ashall, C., Mazzali, P., Bersier, D., et al. 2014, MNRAS, 445, 4427
 Axelrod, T. S. 1980, Ph.D. Thesis California Univ., Santa Cruz.
 Bachetti, M., Harrison, F. A., Walton, D. J., et al. 2014, Nature, 514, 202</p> | <p>Badenes, C., Bravo, E., Borkowski, K. J., & Domínguez, I. 2003, ApJ, 593, 358
 Bikmaev, I., et al. 2015, (Astronomy Letters, submitted)
 Blondin, S., Dessart, L., Hillier, D. J., Khokhlov, A. M. 2013, MNRAS, 429, 2127
 Brown, P. J., Smitka, M. T., Wang, L., et al. 2015, ApJ, 805, 74
 Chugai, N. N. 2000, AstL, 26, 797
 Churazov, E., Gilfanov, M., Forman, W., & Jones, C. 1996, ApJ, 471, 673</p> |
|---|--|

TABLE 8
PAIRWISE COMPARISON OF MODELS FROM TABLE 2. FOR EACH MODEL THE MAXIMUM DEVIATION $|p_{bf}/\sigma_p|$ WITH RESPECT TO ALL OTHER MODELS IS GIVEN.

Model	ISGRI & SPI(400-1350 keV) Maximum deviation	ISGRI & SPI(70-1350 keV) Maximum deviation
No source	9.0	11.1
DDT1p1	0.7	1.8
DDT1p4halo	1.1	2.1
DDTe	2.2	3.6
DETO	12.5	12.6
HED6	4.3	5.4
W7	0.8	1.3
ddt1p4	2.3	1.3
DD4	1.6	1.0

NOTE. — The ISGRI and SPI data for the **early** and **late** period are used jointly. Large deviations imply that the model is disfavored by the data. Using a threshold of 2 standard deviations one can conclude that **No source**, **DETO**, **HED6** and (marginally) **DDTe** models are disfavored by the data, while other models are compatible with the data. Since **3Dbba1** model that was designed to fit the *INTEGRAL* data in the **early** period, this model has been excluded from this test.

- Churazov, E., Sazonov, S., Tsygankov, S., Sunyaev, R., & Varshalovich, D. 2011, MNRAS, 411, 1727
- Churazov, E., Sunyaev, R., Grebenev, S., et al. 2014a, The Astronomer's Telegram, 5992, 1
- Churazov, E., Sunyaev, R., Sazonov, S., Revnivtsev, M., & Varshalovich, D. 2005, MNRAS, 357, 1377
- Churazov, E., Sunyaev, R., Isern, J., et al. 2014b, Nature, 512, 406
- Clayton, D. D., Colgate, S. A., & Fishman, G. J. 1969, ApJ, 155, 75
- Diehl, R., Siebert, T., Hillebrandt, W., et al. 2014a, Science, 345, 1162
- Diehl, R., Siebert, T., Hillebrandt, W., et al. 2015, A&A, 574, A72
- Dong, S., Katz, B., Kushnir, D., & Prieto, J. L. 2014, arXiv:1401.3347
- Dotani, T., Hayashida, K., Inoue, H., Itoh, M., & Koyama, K. 1987, Nature, 330, 230
- Dwarkadas, V. V., & Chevalier, R. A. 1998, ApJ, 497, 807
- Fink, M., Kromer, M., Seitzzahl, I. R., et al. 2014, MNRAS, 438, 1762
- Foley, R. J., Fox, O. D., McCully, C., et al. 2014, MNRAS, 443, 2887
- Fossey, J., Cooke, B., Pollack, G., Wilde, M., & Wright, T. 2014, Central Bureau Electronic Telegrams, 3792, 1
- Friesen, B., Baron, E., Wisniewski, J. P., et al. 2014, ApJ, 792, 120
- Goobar, A., Johansson, J., Amanullah, R., et al. 2014, ApJ, 784, L12
- Goobar, A., Kromer, M., Siverd, R., et al. 2015, ApJ, 799, 106
- Graham, M. L., Foley, R. J., Zheng, W., et al. 2015, MNRAS, 446, 2073
- Greco, J. P., Martini, P., & Thompson, T. A. 2012, ApJ, 757, 24
- Hillebrandt, W., & Niemeyer, J. C. 2000, ARA&A, 38, 191
- Hoeflich, P., & Khokhlov, A. 1996, ApJ, 457, 500
- Hoyle, F., & Fowler, W. A. 1960, ApJ, 132, 565
- Iben, I., Jr., & Tutukov, A. V. 1984, ApJS, 54, 335
- Imshennik, V. S., & Dunina-Barkovskaya, N. V. 2005, Astronomy Letters, 31, 528
- Isern, J., Jean, P., Bravo, E., et al. 2013, A&A, 552, A97
- Isern, J., Knoedlseder, J., Jean, P., et al. 2014, The Astronomer's Telegram, 6099, 1
- Isern, J., et al. 2015, (A&A, submitted)
- Jourdain, E., & Roques, J. P. 2009, ApJ, 704, 17
- Karachentsev, I. D., & Kashibadze, O. G. 2006, Astrophysics, 49, 3
- Kawabata, K. S., Akitaya, H., Yamanaka, M., et al. 2014, ApJ, 795, LL4
- Kelly, P. L., Fox, O. D., Filippenko, A. V., et al. 2014, ApJ, 790, 3
- Kushnir, D., Katz, B., Dong, S., Livne, E., & Fernández, R. 2013, ApJ, 778, LL37
- Kuulkers, E. 2014, The Astronomer's Telegram, 5835, 1
- Lebrun, F., Leray, J. P., Lavocat, P., et al. 2003, A&A, 411, L141
- Leloudas, G., Stritzinger, M. D., Sollerman, J. et al. 2009, A&A, 505, 265
- Maeda, K., Taubenberger, S., Sollerman, J., et al. 2010, ApJ, 708, 1703
- Maeda, K., Benetti, S., Stritzinger, M. et al. 2010, Nature, 466, 82
- Malone, C. M., Nonaka, A., Woosley, S. E., Almgren, A. S., Bell, J. B., Dong, S., & Zingale, M. 2014, ApJ, 782, 11
- Margutti, R., Parrent, J., Kamble, A., et al. 2014, ApJ, 790, 52
- Marion, G. H., Sand, D. J., Hsiao, E. Y., et al. 2015, ApJ, 798, 39
- Matz, S. M., Share, G. H., Leising, M. D., Chupp, E. L., & Vestrand, W. T. 1988, Nature, 331, 416
- Mazzali, P. A., Benetti, S., Altavilla, G. et al. 2005, ApJ, 623, L37
- Milne, P. A., Hungerford, A. L., Fryer, C. L., et al. 2004, ApJ, 613, 1101
- Moll, R., Raskin, C., Kasen, D., & Woosley, S. E. 2014, ApJ, 785, 105
- Motohara, K., Maeda, K., Gerardy, C. et al. 2006, ApJ, 652, L101
- Nadyozhin, D. K. 1994, ApJS, 92, 527
- Nielsen, M. T. B., Gilfanov, M., Bogdán, Á., Woods, T. E., & Nelemans, G. 2014, MNRAS, 442, 3400
- Nomoto, K., Thielemann, F.-K., & Yokoi, K. 1984, ApJ, 286, 644
- Nomoto, K., & Sugimoto, D. 1977, PASJ, 29, 765
- Nugent, P. E., Sullivan, M., Cenko, S. B. et al. 2011, Nature, 480, 344
- Pakmor, R., Kromer, M., Taubenberger, S., Sim, S. A., Roepke, F. K., & Hillebrandt, W. 2012, ApJ, 747, L10
- Patat, F., Taubenberger, S., Cox, N. L. J., et al. 2015, A&A, 577, A53
- Pérez-Torres, M. A., Lundqvist, P., Beswick, R. J., et al. 2014, ApJ, 792, 38
- Piro, A. L., Nakar, E. 2013, ApJ, 769, 67
- Roques, J. P., Schanne, S., von Kienlin, A., et al. 2003, A&A, 411, L91
- Sazonov, S. Y., Lutovinov, A. A., & Krivonos, R. A. 2014, Astronomy Letters, 40, 65
- Shigeyama, T., Nomoto, K., Yamaoka, H., & Thielemann, F.-K. 1992, ApJ, 386, L13
- Seitzzahl, I. R., Ciaraldi-Schoolmann, F., Röpke, F. K., et al. 2013, MNRAS, 429, 1156
- Sturmer, S. J., et al., 2003, A&A, 411, L81
- Sofue, Y. 1998, PASJ, 50, 227
- Sunyaev, R., Kaniovsky, A., Efremov, V., et al. 1987, Nature, 330, 227
- Sunyaev, R. A., Kaniovskii, A. S., Efremov, V. V., et al. 1990, Soviet Astronomy Letters, 16, 171
- Teegarden, B. J., Barthelmy, S. D., Gehrels, N., Tueller, J., & Leventhal, M. 1989, Nature, 339, 122
- Telesco, C. M., Höflich, P., Li, D., et al. 2015, ApJ, 798, 93
- The, L.-S., & Burrows, A. 2014, ApJ, 786, 141
- Ubertini, P., Lebrun, F., Di Cocco, G., et al. 2003, A&A, 411, L131
- Vedrenne, G., Roques, J.-P., Schönfelder, V., et al. 2003, A&A, 411, L63

- Webbink, R. F. 1984, ApJ, 277, 355
- Welty, D. E., Ritchey, A. M., Dahlstrom, J. A., & York, D. G. 2014, ApJ, 792, 106
- Whelan, J., & Iben, I., Jr. 1973, ApJ, 186, 1007
- Winkler, C., Courvoisier, T. J.-L., Di Cocco, G., et al. 2003, A&A, 411, L1
- Woosley, S. E., Kasen, D., Blinnikov, S., & Sorokina, E. 2007, ApJ, 662, 487
- Woosley, S. E., & Weaver, T. A. 1991, in Supernovae (eds Audouze, J., Bludman, S., Mochkovitch, R. & Zinn-Justin, J.) 63-154 (Elsevier, 1991)
- Woosley, S. E., & Weaver, T. A. 1986, ARA&A, 24, 205
- Woosley, S. E., Axelrod, T. S., & Weaver, T. A. 1981, Comments Nucl. Part. Phys., Vol. 9, p. 185 - 197, 9, 185
- Zheng, W., Shivvers, I., Filippenko, A. V., et al. 2014, ApJ, 783, L24